Quaternary Science Reviews 247 (2020) 106543

Contents lists available at ScienceDirect

Quaternary Science Reviews

journal homepage: www.elsevier.com/locate/quascirev

Frequency of exceptional Nile flood events as an indicator of Holocene hydro-climatic changes in the Ethiopian Highlands

Carlo Mologni [a, f, *], Marie Revel [a], Cécile Blanchet [b], Delphine Bosch [c], Anne-Lise Develle [d], François Orange [e], Luc Bastian [a], Lamya Khalidi [f], Emmanuelle Ducassou [g], Sébastien Migeon [a, h]

[a] Université Côte d'Azur, CNRS, Observatoire de la Côte d'Azur, IRD, Géoazur, 06905, Sophia Antipolis, France
[b] GFZ Potsdam, Department of Climate and Landscape Dynamics, Telegrafenberg, 14743, Potsdam, Germany
[c] Géosciences Montpellier, CNRS UMR-5243, Université Montpellier II, 34095, Montpellier, France
[d] Université Grenoble Alpes, Université Savoie Mont Blanc, CNRS, EDYTEM, 73000, Chambéry, France
[e] Université Côte d'Azur, CCMA, 06100, Nice, France
[f] Université Côte d'Azur, CNRS, CEPAM – UMR 7264, 06300, Nice, France
[g] CNRS UMR-5805 EPOC – OASU, Université de Bordeaux, Site de Talence - Bâtiment B18N, 33615, Pessac, France
[h] Sorbonne Université, UFR939, Faculté des Sciences et Ingenierie, Paris, France

ARTICLE INFO

Article history:
Received 15 April 2020
Received in revised form
4 August 2020
Accepted 7 August 2020
Available online 2 September 2020

Keywords:
Nile deep-sea fan
Hyperpycnal flows
Nile flood frequency
African monsoon
African Humid Period
8.2 ka BP event
Centennial resolution

ABSTRACT

Climate conditions in Africa have varied substantially during the Late Quaternary with alternating humid and arid periods controlled mainly by the African monsoonal regime. However, the duration and termination of the last African Humid Period (14–6 ka BP) and its internal climatic variability are still debated. Using a laminated sequence from the Nile Deep-Sea Fan, we reconstruct for the first time the monsoon-induced frequency of exceptional Nile floods at centennial resolution during the African Humid Period. By combining sedimentological, geochemical and microscopic tools and comparing our record with two proximal piston cores and with regional paleoclimatic records, we show: **a**) the occurrence of recurrent high-energy floods between 10.1 and 9 ka BP, during the height of the African Humid Period; **b**) a shift in the hydro-climatic regime as early as 9 ka BP, with a progressive reduction in flood frequency and magnitude until 8.2 ka BP, likely related to a southward migration of the monsoon rainfall belt; **c**) a drastic reduction of flood activity between 8.2 and 7.8 ka BP; **d**) an unstable Ethiopian-Nile hydrological system from 7.8 ka BP, followed by a further decrease in river runoff until ~4 ka BP. The occurrence of a stepwise hydro-climatic deterioration over the Ethiopian Highlands from ~9 ka BP brings into question the climatic linkages and feedbacks between low and high latitudes during the Early to Mid-Holocene and in particular around the 8.2 ka BP North Atlantic cooling event. Our unique record of flood frequency at centennial-resolution therefore allows us to draw new insights on fluvial and geomorphic feedbacks of the Nile hydrologic system to monsoonal regimes during a period of major environmental shifts.

1. Introduction

Monsoons are the dominant seasonal mode of climate variability in the tropics, acting as the main driver of climate worldwide. At present, the tropics concentrate the maximum amount of energy and redistribute it in the form of air and moisture masses to subtropical latitudes between 30°N and 30°S. Hydro-climatic conditions in the current Sahel area (Fig. 1b) have varied in the past following a precessional pacing (i.e., every 21,000 years; Mohtadi et al., 2016). Periods that were more humid in the past compared with present-day conditions have been attributed to the northward migration of the rainfall belt associated with the Inter Tropical Convergence Zone (ITCZ; Mohtadi et al., 2016). This migration is governed by precession-driven insolation changes and modulated by the eccentricity (deMenocal et al., 2000; Gasse, 2000; Rossignol-Strick et al., 1982; Skonieczny et al., 2019). Past humid periods were

* Corresponding author. Université Côte d'Azur, CNRS, Observatoire de la Côte d'Azur, IRD, Géoazur, 06905, Sophia Antipolis, France.
E-mail address: mologni@geoazur.unice.fr (C. Mologni).

https://doi.org/10.1016/j.quascirev.2020.106543
0277-3791/

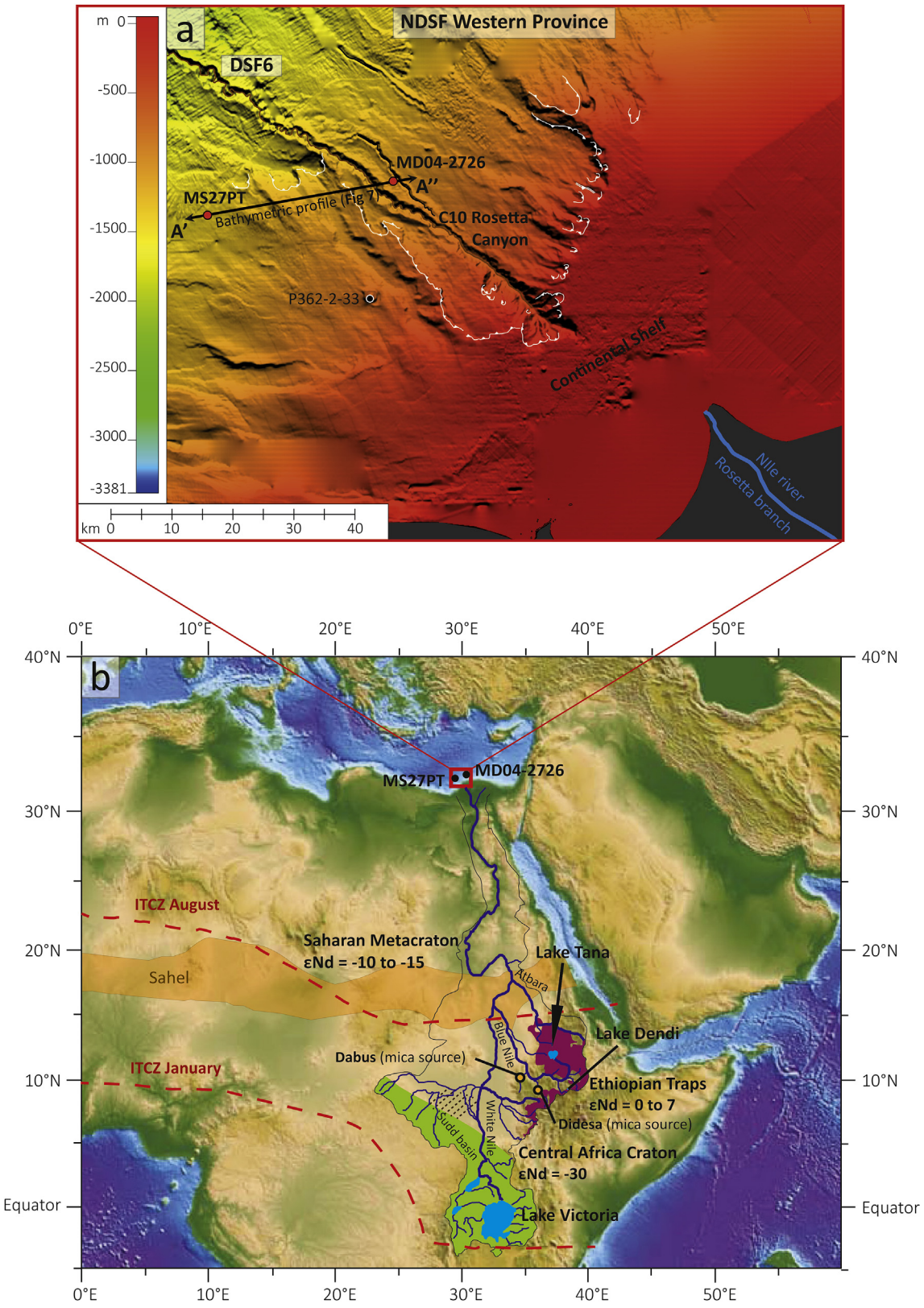

Fig. 1. a) Bathymetric map of the Western Nile Deep Sea Fan (NDSF; proximal Rosetta upper slope, C10 Rosetta canyon, DSF6) showing the locations of the studied cores MD04-2726 (31°51.00′ N, 29°47.49′ E, 1058 m water depth) and MS27PT (N31_47.90'; E29_27.700, 1389 m water depth; red dots), the bathymetric profile presented in Fig. 7, and the P362-2-33 core (Blanchet et al., 2013, black dot). **b**) Hydrological context of North Africa and the present-day active Nile watershed (modified from Skonieczny et al., 2015). Three main sources of suspended sediment load are identified in the Nile Deep-Sea Fan: the basaltic rocks (purple) of the Ethiopian Traps (Highlands), which are drained by the Blue Nile, Atbara and Sobat rivers located at tropical latitude (around 5 to 15°N); the Precambrian metamorphic rocks (green) of the Central African Craton located in the equatorial latitude of Lakes Albert and Victoria in the Ugandan headwaters region of the White Nile; the Saharan Metacraton (Abdelsalam et al., 2002) which produces aeolian dust representing the source region of most deflation documented by (Prospero et al., 2002; Scheuvens et al., 2013). The outcrops of the Ethiopian Traps, Precambrian Craton and Saharan Metacraton provide

characterized by enhanced discharge and sediment export from the large African river systems to surrounding ocean margins. The most recent period of more intense rainfall, the African Humid Period (AHP: from ~14 to ~6 ka BP; Shanahan et al., 2015), led to the expansion of continental water bodies (Gasse, 2000), the development of vegetation cover over the present-day Sahelian-Saharan desert (Hopcroft et al., 2017) and very high riverine-induced terrigenous inputs. Many recent studies conducted at high temporal resolution (100 years) in lake and deltaic sediment records across the East African Rift System and over the North African continental margins suggest that gradual long-term monsoon oscillations (controlled by external orbital forcing) were often punctuated by millennial-scale episodes of hyper aridity (Bastian et al., 2017; Chalié and Gasse, 2000; Costa et al., 2014; Foerster et al., 2012; Tierney and deMenocal, 2013; Verschuren et al., 2009).

The most recent arid episodes occurred during the AHP and at the onset of the AHP (8.2 and 12.8 ka BP), coinciding with the melting of icebergs from the Laurentide ice sheet into the Arctic (Collins et al., 2017, 2011). It has been proposed that the reduction of Atlantic thermohaline circulation could have induced a reduction of African monsoon activity (Mulitza et al., 2008). In order to understand the mechanisms linked to these abrupt climate changes between low and high latitudes, it is crucial to work on natural archives with a centennial to decadal temporal resolution.

The main goal of this work is to investigate Nile river discharge over the last ~10.3 thousand years at a centennial time resolution, with the aim of documenting the internal dynamics of the AHP in East Africa. A particular focus will be set on the 8.2 ka BP arid event, to better understand the timing, mechanism and feedback of African monsoon activity in the Ethiopian-Nile basin.

Sediment deposition in deltas is dominated by terrigenous material delivered from flooding rivers and is highly sensitive to changes in precipitation rate and the extension of vegetation cover in drainage basins. The sediment records preserved in the Nile Deep-Sea Fan (NDSF) provide suitable archives for reconstructing past continuous climate variations (Ducassou et al., 2009). Previous studies on the NDSF have demonstrated that past humid periods were systematically accompanied by higher deposition rates and enhanced terrigenous supply, reflecting strong physical erosion and transport processes from the Ethiopian Highlands related to African monsoon activity (Blanchet et al., 2014; Ducassou et al., 2009; Krom et al., 2002; Revel et al., 2010, 2014, 2015). In addition, the provenance of particles exported to the NDSF has been inferred from the application of Nd and Sr radiogenic isotopes in sediment cores (See section 2.2).

Over the NDSF, the variability of lithological facies includes pelagites/hemipelagites, turbidites, debrites, slide/slump deposits and clastic muds (Ducassou et al., 2009, 2008; 2007; Migeon et al., 2010). During strong flood events, fine-to coarse-grained beds named hyperpycnites can be deposited at ocean and sea margins (Mulder et al., 2003, 2001; Parsons et al., 2001). However, in the NDSF, Nile flood events seem to be recorded through the emplacement of the so-called “clastic-mud beds” (Ducassou et al., 2008; Revel et al., 2010; Blanchet et al., 2013). The deposition of these beds is explained by the reconcentration of surface plumes originating from terrigenous river discharge by convective processes leading to the formation of hyperpycnal flows at depth (Ducassou et al., 2008; Parsons et al., 2001).

In this study, we focus on well-preserved turbidite beds located in the Western Province of the NDSF (MD04-2726 core, Fig. 1), that we interpret to be a potential instantaneous and direct record of the Nile-river floods during the AHP, related to African paleo-monsoon activity.

Integrating multiproxy sedimentological and geochemical (major elemental and Nd isotopes) data, we address four challenges: **a**) distinguishing between beds deposited by hyperpycnal flows and those induced by failure-triggered gravity flows or by density convective processes (clastic-mud beds) along the Rosetta Canyon and the continental slope; **b**) confirming the coherency of these hyperpycnal-flow deposits over the western NDSF by comparing them with similar laminated and well-dated records in the Rosetta System (MS27PT and P3622-33 cores; Revel et al., 2015; Blanchet et al., 2013, respectively); **c**) characterising the frequency and magnitude of Nile paleo-floods over the last 10.1 kyr; and **d**) finally, discussing the meaning of Nile-flood frequencies at centennial resolution and their links with paleo-monsoon activity during the AHP, with a particular focus on the Early to Mid-Holocene and on the 8.2 ka BP hyper-arid event (Rohling and Pälike, 2005).

These results will be of interest to better constrain identification of hyperpycnal-flow deposits within mud-prone turbidite systems similar to the Nile Deep-Sea Fan and to better constrain African paleo-monsoon dynamics for integration within broader climate modelling.

2. Regional settings

2.1. The NDSF Western Province morphology

Core MD04-2726 was collected in the upper part of the Rosetta Turbidite System, located on the western NDSF (Ducassou et al., 2009; Mascle et al., 2006), off the Rosetta branch of the Nile subaerial delta (Fig. 1a). Here, the continental shelf is about 30 km wide, and the head of the Rosetta Canyon lies on the outer continental shelf at a water depth of about 70 m (Fig. 1a). It is about 25 km long and 200–250 m deep, and is straight following the main slope angle of the continental slope. In cross section, the Rosetta Canyon is characterized by U- to poorly-developed V-shaped profiles where a large number of small-scale failures affected the canyon flanks (Fig. 1a). The Rosetta Canyon connects to a meandering channel-levee system named DSF6, which was initiated during Marine Isotopic Stage 3 (MIS 3) (Ducassou et al., 2009) and potentially recorded the Holocene activity of the Nile flood-induced inputs.

2.2. The NDSF Western Province sediment sources

The sedimentary provenance of terrigenous material in the western NDSF can be characterized through its neodymium isotopic signature (εNd) (Bastian et al., 2017; Blanchet et al., 2014; Blanchet, 2019; Migeon et al., 2010; Revel et al., 2010; Weldeab et al., 2002). Since the Nile basin encompasses the Precambrian African basement as well as the Cenozoic Ethiopian traps, which have contrasting Nd isotopic compositions, geochemical studies on its sediment loads allow us to distinguish between the sources of the material (Fig. 1b). 96% of the particles deposited in the NDSF today are estimated to originate from the Blue Nile and Atbara rivers and only 4% from the White Nile (Be'eri-Shlevin et al., 2018;

sediments characterized by εNd values of >0, > −30 and from −10 to −14 respectively (Garzanti et al., 2015; Grousset and Biscaye, 2005; Skonieczny et al., 2011). The seasonal positions of the Intertropical Convergence Zone (ITCZ; red dotted line, Viste and Sorteberg, 2013) as well as of the Sahel zone (orange area) are shown, as well as the Nile catchment mica sources (Dabus and Diesda rivers, orange dots; after Garzanti et al., 2015). (For interpretation of the references to colour in this figure legend, the reader is referred to the Web version of this article.)

Garzanti et al., 2015; Padoan et al., 2011). The Bahr el Jebel and Victoria-Albert Nile-derived fluvial muds are characterized by εNd (0) ≈-25 (Padoan et al., 2011), whereas the White Nile mud reaching Khartoum could have a Saharan Metacraton imprint with εNd around −13 (Fig. 1b; Skonieczny et al., 2011). Aeolian dust from the western to central Saharan region are characterized by relatively constant values of εNd ranging between −10 and −15 (Grousset and Biscaye, 2005; Scheuvens et al., 2013).

Thus, temporal changes in both Nd signature and sedimentation rate from sedimentary records in the NDSF allow us to track past temporal changes in relative proportions of detrital sediment originating from the Ethiopian Traps located in tropical latitudes between 5°N and 15 °N (εNd > 0), the Central Africa Craton located in equatorial latitude (εNd ≈ −30), and the Saharan Metacraton located in the present Sahara (Abdelsalam et al., 2002) and which is an important aeolian dust producer (εNd ≈ −10 to −15).

3. Materials and methods

The present study is based on the analysis of the MD04-2726 core (N 31°51.00′, E 29°47.49') collected during the VANIL campaign (2004). The total MD04-2726 piston core length measures 26.5 m and is composed of 18 sections. Because of the good preservation of the hyperpycnite sequence and according to the aim of this and previous studies (Revel et al., 2015) we focused our investigation on the upper five sections (732 cm; Fig. 2e). The core was extracted on the right-hand levee of the upper Rosetta Channel at a water depth of 1058 m (Fig. 1a), and represents the closest core from the coastline to have been collected on the Nile margin, i.e. <60 km away from the Rosetta-river mouth. This core is characterized by high accumulation rates and thus provides high-resolution temporal information on the links between hydroclimate and erosion processes on continents.

Identification of individual depositional beds was based on the integration of various methods including visual description at millimetre scale, grain-size, XRF-CS, Nd isotopic composition and thin-section analyses that are described below.

3.1. AMS ^{14}C measurements

The age model of the MD04-2726 sequence was constructed using thirty Accelerator Mass Spectrometry (AMS) ^{14}C dates (Table 1). In order to improve the age model for core MD04-2726 (Revel et al., 2015), a set of 18 additional radiocarbon ages was obtained (Table 1, Fig. 2a). The scarcity of planktonic foraminifera shells in sections III-IV-V precludes the addition of new radiocarbon measurement on biogenic carbonates. We therefore obtained seven new AMS ^{14}C measurements on bulk organic matter (bulk OM) for this part of the core and 11 new AMS ^{14}C measurements of planktonic foraminifera shells in sections I-II-III (Fig. 2, Table 1).

Calibrated ages were obtained with the OxCal software (v4.3.2, Bronk Ramsey, 2017), while the age-depth modelling was performed using the Bacon software (v3.6.3, Blaauw and Christen, 2011). Conventional ages on foraminifera assemblages were calibrated using the MARINE13 calibration curve, which includes a mean global reservoir correction of 400 yrs (Reimer et al., 2013; Siani, 2001). Paired measurements of AMS ^{14}C of planktonic foraminifera and bulk OM on the same depth interval (658 cm, section V; Table 1) allows us to estimate the age reservoir correction of the continental OM. Inversely to classical methods to determine the local age reservoir for marine sediments (Dewar et al., 2012; Reimer et al., 2002; Reimer and Reimer, 2017), we used the calibrated age of planktonic foraminifera (to MARINE13, 9736 cal yr BP) to determine the apparent age of contemporaneous organic matter (from IntCal13, 8766 cal yr BP) and calculated the difference with the radiocarbon age of bulk OM (10,620 yr BP). The calculated offset of 1854 yr was used as a constant reservoir age to correct all radiocarbon ages on organic matter (Table 1). Owing to the dominantly continental origin of bulk OM in sediments from the NDSF deposited during the African Humid Period (Blanchet et al., 2014; Ménot et al., 2020), the ages on bulk OM and on organic macro-remains were calibrated using the IntCal13 curve (Reimer et al., 2013). The reliability of the age model and inherent limitations will be further discussed in section 4.1.

3.2. XRF core scanner on soft sediment

X-Ray fluorescence core scanning (XRF-CS) was performed using an Avaatech core scanner at the EDYTEM laboratory (CNRS-Université de Savoie Mont-Blanc). The XRF-CS analyses were performed on core MD04-2726 with a 1 mm sampling step and with a 10 kV voltage (Al, Si, S, K, Ca, Ti, Mn, Fe) for sections I-II (Revel et al., 2015), and with a 10 KV and 30 kV voltage (Al, Si, S, K, Ca, Ti, Mn, Fe; Cu, Zn, Br, Sr, Rb, Zr, Pb) for sections III-IV-V (this study). Each individual power spectrum was transformed by deconvolution into relative contents (intensities) expressed in counts per seconds (cps). In this study we principally used the logs of elemental ratios, following a well-established methodology to circumvent problems associated with the closed-sum constraints (Croudace and Rothwell, 2015; Weltje and Tjallingii, 2008).

A principal component analysis (PCA) was performed on geochemical results using the R® software. This statistical procedure uses an orthogonal transformation to convert a set of observations of possibly correlated variables (our elements) into a set of values of linearly uncorrelated variables called principal components (dimensions). This analysis has been thus applied to XRF results in order to decipher sedimentary processes controlling MD04-2726 geochemical variations (Sup. Mat. Figure S1).

3.3. Particle grain size analysis and LOI

Grain-size analyses were performed using a Coulter-LS2000 following two sampling strategies: **a**) a centimetre-scale sampling step over the total core length (733 cm); **b**) a millimetre-scale sampling step (2 mm) in selected individual beds identified using the mm-XRF major elemental variation and centimetre-resolution grain-size distribution data. To avoid clay flocculation and to dissociate mineral particles, we used sodium hexametaphosphate (NaHMP) and ultrasonic treatment. Sediment was previously decarbonated (HCl, 1 mol), while the organic matter was maintained (no H_2O_2 dissolution), considered as a grain-size marker of river-induced instantaneous deposits. SEM and light microscopic qualitative analyses on this section and on bulk decarbonised sediment (see 3.4 for methodology) showed the near-absence of diatom frustules, which are thus considered as a negligible factor for grain-size measurements and interpretations.

We determined the grain-size of the intercepts for 10%, 50% and 90% of the cumulative grain-size curves (named Q90, Q50 and Q10 values; Folk and Ward, 1957). The ratio Q90/Q10 is used to identify the coarser-grained beds (hyperpycnites) along the studied interval, while the Q90/Q50 ratio and Gaussian curves are used to discriminate between the bed types and to propose a hydrodynamic interpretation.

Loss On Ignition (LOI) was performed on 2 g sediment samples by heating for 24 h at 100 °C for residual water and gypsum content and then 4 h at 550 °C for organic carbon total content measures (Santisteban et al., 2004).

3.4. Light and electron microscopy analyses

Microscopic analyses were performed on 11 thin sections sampled in selected individual beds (Fig. 3). Thin sections were analysed using the Zeiss Axioskop 40 Pol/40 petrographic microscope with UV light used to detect phosphate materials. Pictures of total thin sections presented in this article were obtained from high-resolution transmission scanning in crossed (XPL) and direct polarized light (PPL).

Qualitative and semi-quantitative geochemical analysis on uncovered thin sections was performed using scanning electron microscopy (SEM). SEM was also used for the surface textural analyses of quartz grains, following Vos et al. (2014) sampling processing and analysis settings. SEM observations and Energy Dispersive X-Ray spectroscopy (EDX) analyses were carried out with a Tescan Vega3 XMU scanning electron microscope (TESCAN FRANCE, Fuveau, France) equipped with an Oxford X-MaxN 50 EDX detector (Oxford Instruments, Abingdon, U.K.). Thin sections were observed and analysed with no prior metal or carbon coating, using the low vacuum mode (N2 pressure ~35 Pa) and at a 20 kV accelerating voltage. Imaging was performed using backscattered electrons. EDX spectra were processed with the Aztec software (version 3.1, Oxford Instruments). Surface textural analyses of quartz grains were performed on 10 to 20 grains for each of the beds identified in thin sections, with a grain-size range between 100 μm and 1 mm, randomly selected under a binocular microscope and then analysed using the SEM. Quartz grains were coated with platinum (3 nm) prior to SEM observations at a 5 kV accelerating voltage.

3.5. Nd radiogenic isotope analyses

Isotope ratios were measured on carbonate-free <63 μm particle size both on hemipelagic and turbidite deposits, using 100 mg of the dried aluminosilicate fraction. Chemical extractions for Nd isotopes were carried out at the Laboratory of Geoscience Montpellier. Samples were leached for 1 h with 1 N HCl to dissolve biogenic carbonates. The Fe–Mn oxyhydroxide fraction and organic carbon were removed using 10 ml 1 M Hydroxylamine hydrochloride and 10 ml 5% H_2O_2, respectively (Bayon et al., 2002). After leaching, the samples were centrifuged and the supernatant discarded. The remaining sediment was washed three times with ultra-pure water, discarding the supernatant each time to remove the biogenic components and to eliminate any marine Nd isotope signal adsorbed on to the silt-clay fraction. The chemical separation of Nd included a first separation step using AG50W-X-8 cation exchange resin to collect rare earth elements followed by purification of Nd using HDEHP conditioned Teflon columns. Nd isotopes were measured using a Thermo Scientific Neptune Plus MC-ICP-MS from the AETE-ISO geochemical platform (OSU-OREME, Montpellier University). The $^{143}Nd/^{144}Nd$ isotopic compositions were corrected for internal mass bias using an exponential law and a value of 0.7219 for the $^{146}Nd/^{144}Nd$ ratio. The external mass bias was corrected using the standard bracketing method using AMES-Rennes and analysing each of the 2 unknowns. During the course of the study AMES-Rennes standards yielded an average 0.511946 ± 6 (2σ, n = 10) for the $^{143}Nd/^{144}Nd$ ratio (Chauvel and Blichert-Toft, 2001). The Nd procedural blank measured during the course of this study was 25 pg. Epsilon Nd values (εNd) were calculated using $^{143}Nd/^{144}Nd = 0.512638$ (Bouvier et al., 2008).

4. Results

4.1. Age model, lithology and sedimentation rates

According to the age model, the upper 7.3 m of core MD04-2726 span the last 10 kyr, covering the Holocene period (Fig. 2a). Both the range (between 0.2 and 3.5 mm/yr) and the timing of changes in sedimentation rates are coherent with previous reports from nearby archives (Blanchet et al., 2013; Revel et al., 2014, 2015; Hennekam et al., 2015). A large variability in radiocarbon ages (including several reversals) is observed in sections III-IV-V, where the highest sedimentation rates are computed (>1 mm/yr). This is probably related to unaccounted changes in the reservoir age of bulk OM through time, due to varying proportion of terrestrial and marine OM in the sediments as well as to the incorporation of terrestrial OM of varying ages. Complex interplay between storage and erosion processes in fluvial basins can indeed lead to the release of pre-aged OM as old as 2000 yrs, as shown by Schefuβ et al. (2016) for the Congo River. A reservoir age of ~1200 yr has been obtained for a layer dated at ca. 9 ka BP in nearby core P362/2–33 (unpublished results, C. Blanchet), which is 650 yrs younger than the reservoir age of ~1850 yrs obtained for core MD04-2726 at ca. 9.8 ka BP. We therefore consider that uncertainties on radiocarbon ages obtained on bulk OM associated with likely variations in reservoir age through time are in the order of ~500 yrs. For all other ages, uncertainties range between ~30 and ~100 yr, see Table 1). Accounting for these inherent limitations and for the generally lower temporal resolution of regional records, we limit our interpretations to centennial-scale changes.

Based on the lithology, four sedimentological intervals were identified in core MD04-2627, depicted here from bottom to top. The first interval lies between 732 and 700 cm and is dated between ~10.3 and ~10.1 ka BP (Fig. 2a). It is composed of muddy non-laminated sediment (Fig. 2e). The second interval ranges from 700 to 132 cm and is dated between ~10.1 and ~7.2 ka BP. It is characterized by sandy-silt to silty-mud turbidites and laminated hemipelagic muddy beds, with sedimentation rates between ~1 and ~3.5 mm/yr. The total carbonate content never exceeds 10%. The whole interval corresponds to the Sapropel S1, formed under anoxic bottom-waters conditions which circumvented the bioturbation (Thomson et al., 1999). Thus we observe a high organic content (8–9%; Fig. 4a), low Mn/Al values (Fig. 2d) and the lack of bioturbation features. The third interval lies between 132 and 70 cm and is dated between ~7.2 and ~5.8 ka BP (Fig. 2a). It represents the transition from sapropelic to pelagic conditions with no turbidite beds, corresponding to the increase of deep and intermediate water ventilation in the Eastern Mediterranean during the termination of the AHP. The fourth interval corresponds to the upper 70 cm and spans the last 5.8 kyr. A reduction of S/Cl (Revel et al., 2015) and two peaks of Mn/Al ratio at 6.8 and 4.3 ka BP mark the reestablishment of Mid-Holocene oxic conditions (Fig. 2d; De Lange et al., 2008). This interval has a sedimentation rate of ~0.15 mm/yr (Fig. 2a) and consists of yellowish-brown bioturbated pelagic mud devoid of turbidite beds with a great number of planktonic foraminifera.

4.2. Nd isotopic composition

In core MD04-2726, εNd values measured on the <63 μm silicate fraction range between −2 and −6 and three isotopic trends are distinguished (Fig. 2b). Values of εNd between −2.5 and −4 are observed between 700 and 400 cm, indicating a larger proportion of particles derived from the Ethiopian Traps. These are followed by values of εNd between −4 and −5 observed between 400 and 70 cm. Finally, distinctly low εNd values (<-5.5) are measured between 70 and 20 cm in phase with the low values of the Ti/Ca ratio. εNd values from turbiditic beds show a systematic offset by ~ +0.6 compared to the hemipelagic facies (Fig. 2b).

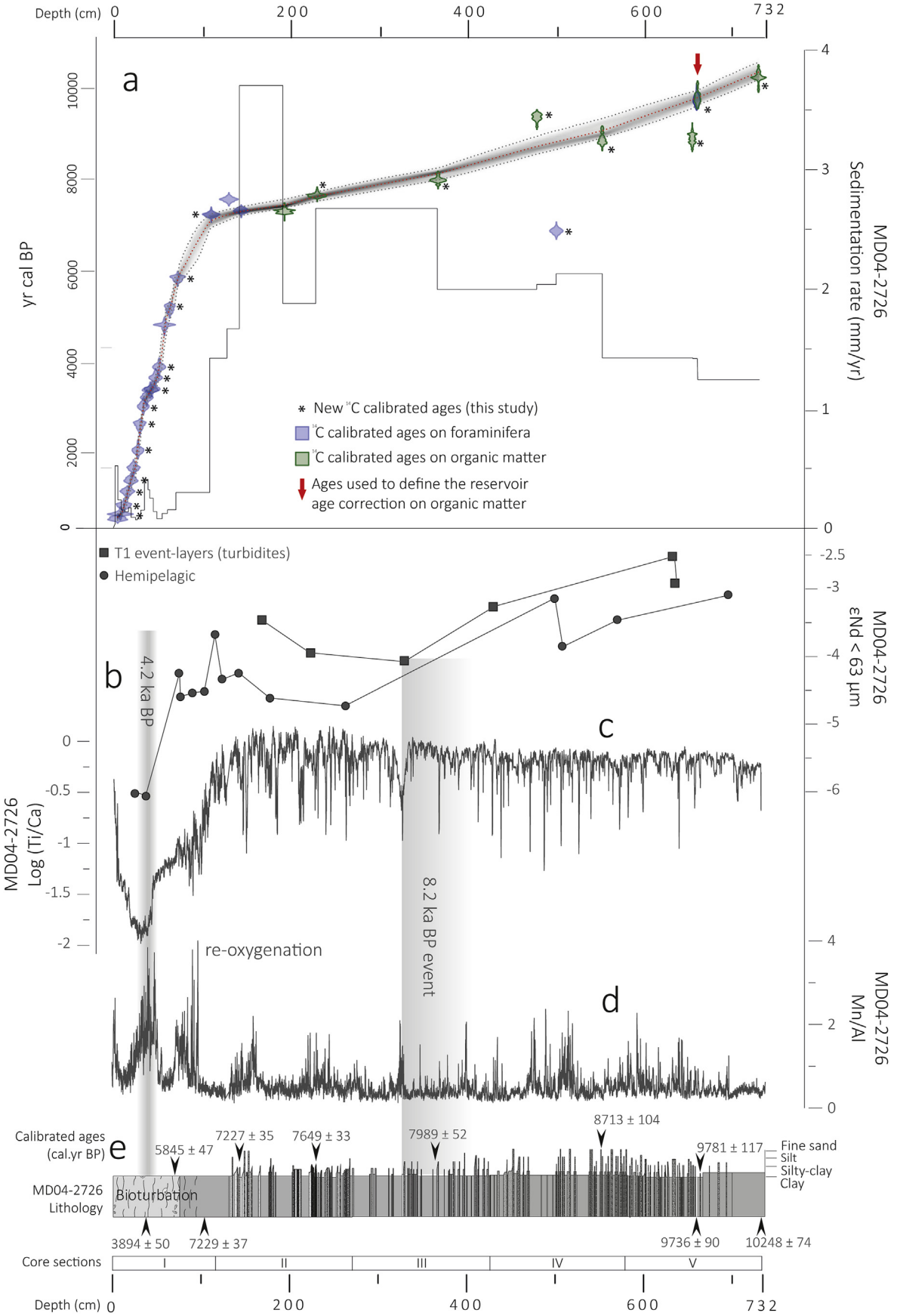

Fig. 2. a) Age model of the MD04-2726 core with new (asterisk, this study), and previous (Revel et al., 2015) ^{14}C calibrated ages, indicating ages obtained on foraminifera (blue tie points) and on organic matter (green tie points); sedimentation rate (mm/yr) of the MD04-2726 core. **b**) Silt (<63 μm) εNd values of T1 event-layers (squares) and hemipelagic sediments (dots) of the MD04-2726 core. **c**) Log (Ti/Ca) and **d**) Mn/Al ratios from 1 mm resolution XRF core scanner measurements from the MD04-2726 core. **e**) Lithology and texture of the MD04-2726 core with indicated section depths and the localisation of new and previous calibrated ages. (For interpretation of the references to colour in this figure legend, the reader is referred to the Web version of this article.)

Table 1
Calibration of new and previous ages on MD04-2726 core, and results from age model building using the Bacon software (v3.6.3, Blaauw and Christen, 2011) based on Marine13 and IntCal13 calibration curves (Reimer et al., 2013). Bulk OC = Bulk Organic Carbon; * = new ages (this study).

Lab. Code	Depth (cm)	Material	Radiocarbon age (^{14}C yr BP± 1σ)		Carbon content (mg)	Reservoir correction (yr)	Cal Curve	Calibrated age (cal yr BP ± 2σ)	Bacon median age (cal. yr BP ± 2σ)
SacA16520	2	G. ruber alba	970	±30	0.8	0	Marine13	564 ± 32	601 ± 71
SacA53733 *	5	Planktonic for.	1115	±30	0.44	0	Marine13	670 ± 28	662 ± 62
SacA53734*	9	Planktonic for.	1315	±30	0.59	0	Marine13	858 ± 41	829 ± 100
SacA53735 *	13	Planktonic for.	1595	±30	0.94	0	Marine13	1162 ± 46	1094 ± 177
SacA53736 *	17	Planktonic for.	1865	±30	0.72	0	Marine13	1409 ± 47	1392 ± 204
SacA16521	20	G. ruber alba	2105	±30	1.2	0	Marine13	1684 ± 52	1568 ± 227
SacA53737 *	25	Planktonic for.	2425	±35	1.02	0	Marine13	2062 ± 55	2136 ± 152
SacA53738 *	27	Planktonic for.	2855	±30	1.03	0	Marine13	2633 ± 61	2435 ± 312
SacA35503*	31	G. ruber alba	3220	±30	1.28	0	Marine13	3028 ± 56	2986 ± 158
SacA22281	35	G. ruber alba	3365	±30	0.96	0	Marine13	3229 ± 52	3226 ± 98
SacA53739*	39	Planktonic for.	3505	±30	0.95	0	Marine13	3398 ± 40	3360 ± 89
SacA22280	41	G. ruber alba	3525	±30	0.99	0	Marine13	3409 ± 41	3425 ± 99
SacA53740 *	45	Planktonic for.	3735	±30	1.04	0	Marine13	3657 ± 52	3582 ± 139
SacA53741 *	49	Planktonic for.	3915	±30	0.78	0	Marine13	3894 ± 50	3877 ± 218
SacA22279	55	G. ruber alba	4590	±30	0.69	0	Marine13	4813 ± 41	4651 ± 318
SacA53742 *	61	Planktonic for.	4870	±30	0.64	0	Marine13	5186 ± 66	5260 ± 236
SacA16523	70.5	G. ruber alba	5465	±30	0.26	0	Marine13	5845 ± 47	5801 ± 154
SacA35504 *	108.5	G. ruber alba	6700	±30	0.61	0	Marine13	7229 ± 37	7100 ± 158
SacA16524	128	G. ruber alba	7085	±35	0.3	0	Marine13	7564 ± 38	7233 ± 123
SacA35505	142	Bulk for.	6790	±30	1.11	0	Marine13	7317 ± 40	7300 ± 87
SacA38937	191	Vegetal macrorest	8160	±30	0.751	1854	IntCal13	7227 ± 35	7445 ± 52
Poz-108962 *	228	Bulk OC	8670	±40	0.873	1854	IntCal13	7649 ± 33	7629 ± 103
Poz-108961 *	365	Bulk OC	9020	±50	0.477	1854	IntCal13	7989 ± 52	8130 ± 151
Poz-108959 *	477	Bulk OC	10,210	±50	0.973	1854	IntCal13	9380 ± 66	8707 ± 152
SacA53743 *	499	Planktonic for.	6395	±30	0.46	0	Marine13	6870 ± 49	8804 ± 148
Poz-108958 *	551	Bulk OC	9720	±50	0.759	1854	IntCal13	8713 ± 104	9070 ± 111
Poz-105356 *	653	Bulk OC	9890	±50	2.391	1854	IntCal13	8897 ± 94	9743 ± 182
SacA16525	658	G. ruber alba	9045	±45	0.6	0	Marine13	9736 ± 90	9785 ± 159
Poz-105342 *	658.5	Bulk OC	10,620	±50	2.014	1854	IntCal13	9781 ± 117	9793 ± 160
Poz-105341 *	728	Bulk OC	10,930	±60	2.891	1854	IntCal13	10248 ± 74	10353 ± 153

4.3. Description of T1 and T2 event-layers

The integration of sedimentological and geochemical data allows the identification at millimetre-scale of 102 coarser grain-size beds within the sapropelic interval (~7.2—~10.1 ka BP; Fig. 3a). Two types of beds are distinguished: 83 are characterized by an increase of Ti/K, Mn/Al and Q90/Q10 ratio (T1 event-layers; Figs. 3, 4 and 6) and 19 are characterized by an increase of both the Ti/K and Q90/Q10 ratios, without Mn/Al peaks (T2 event-layers; Figs. 3, 5 and 6).

4.3.1. T1 event-layer description

T1 event-layers (1–6 cm thick) are characterized by a mixed grading, consisting of a basal inverse grading overlaid with an upper normal grading (Fig. 4a). Each T1 bed consists of the superposition of a maximum of 5 facies named I to V from base to top (Fig. 4a).

The Facies I (Fig. 4a) consists of a basal coarsening-upward unit with high amounts of clay minerals. Organic-matter micro-remains of continental origin and primary minerals (micas >20 μ) are also

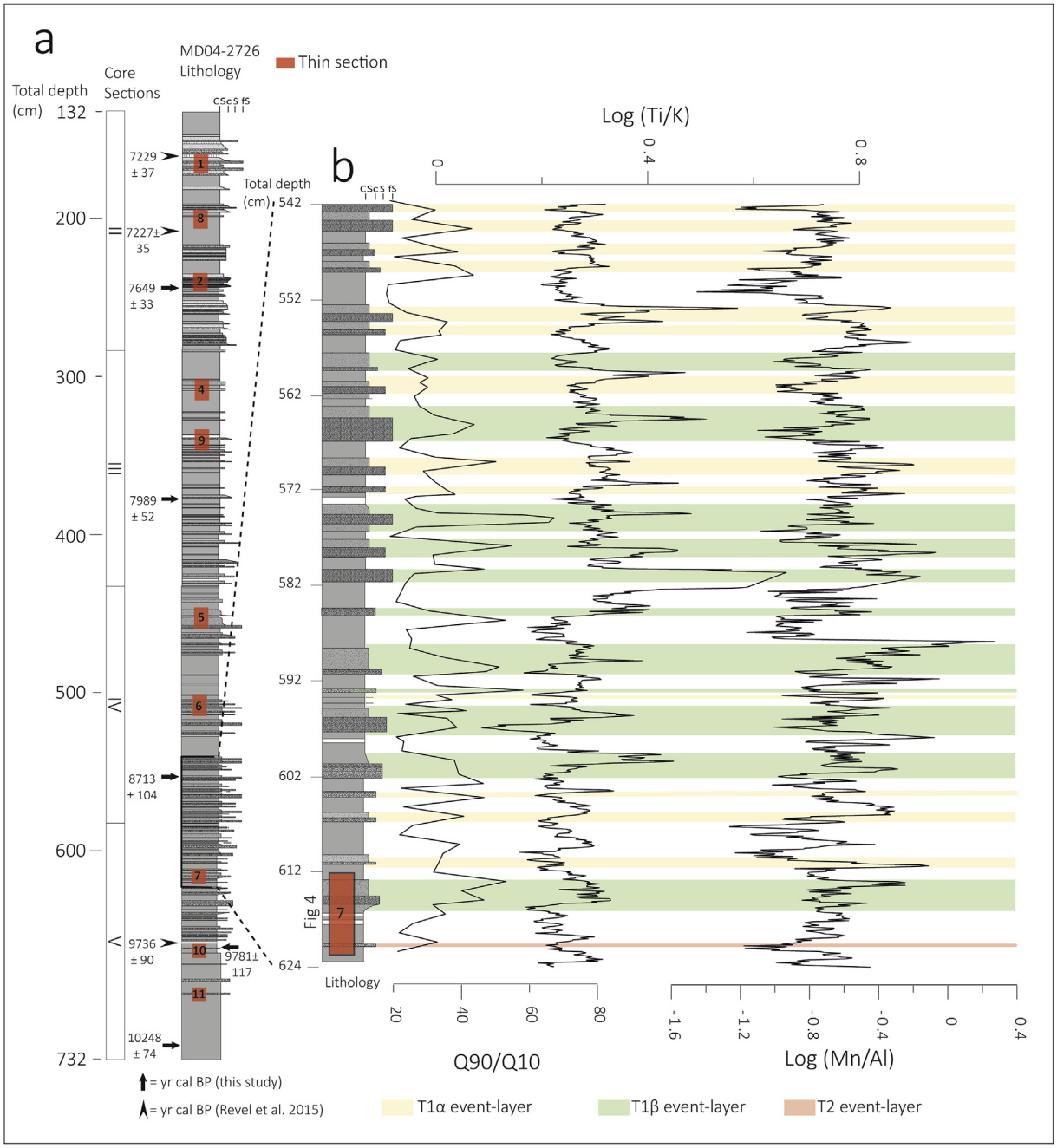

Fig. 3. a) Lithology and texture of the turbidity sequence in core MD04-2726 (sections II to V), with the location of the sampled and studied thin sections (orange boxes) and of new and previous calibrated radiocarbon ages (see Fig. 2). **b**) Detail of the lithology for the interval 542–624 cm depth with the location of thin section N°7 (orange box, see Fig. 4), the Q90/Q10 and Log (Ti/K) and Log (Mn/Al) ratios. The T1α, T1β and T2 event-layers are identified by yellow, green and red highlights, respectively. (For interpretation of the references to colour in this figure legend, the reader is referred to the Web version of this article.)

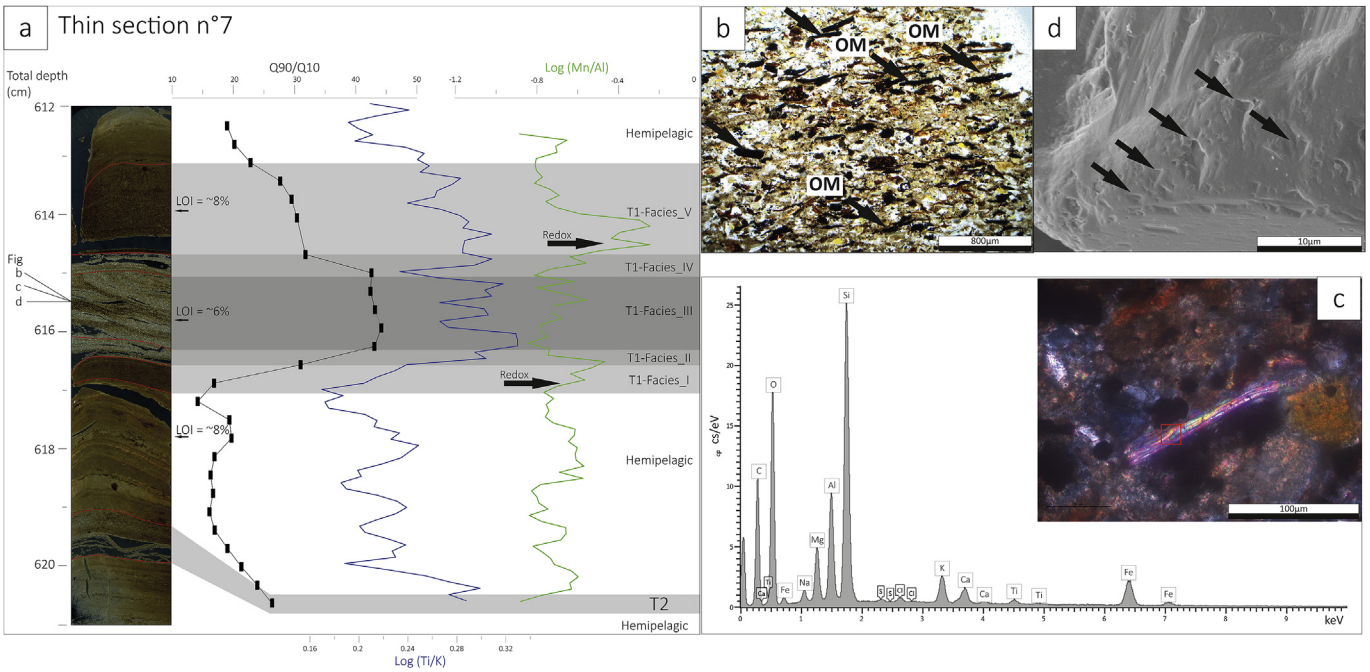

Fig. 4. a) Scan in crossed polarized light of thin section N°7 with the location of Fig. 4b, c and 4d, the T1 Facies (I to V), and the T2 and hemipelagic facies; Q90/Q10 (black line), Log (Ti/K) (blue line) and Log (Mn/Al) (green line); black arrows indicating the fluvial-induced redox facies; LOI (%) over hemipelagic and T1 sedimentary facies. **b**) SEM image in plane polarized light of T1 Facies III showing the organic matter (OM, black arrows) with horizontal orientation and distribution patterns in climbing ripple sedimentary patterns; **c**) SEM image in crossed polarized light of T1 Facies III showing a non-weathered mica mineral with the respective EDX analysis spectrum. **d**) SEM image of quartz grain surface showing small to large conchoidal microfractures and V−shaped percussion cracks (black arrows). (For interpretation of the references to colour in this figure legend, the reader is referred to the Web version of this article.)

present and they coarsen from the bottom to the top of the facies. Facies I is poorly laminated, with an alternation between muddy and silty laminae, the latter thickening upward (Fig. 4a). Together with an inverse grading, Facies I exhibits a gradual upward increase of the Ti/K ratio (Fig. 4a). Facies II is characterized by a sharp basal contact, the disappearance of clay and fine-silt fractions and an increase in grain-size (Fig. 4a). Horizontal parallel laminations are present, with a coarsening-up pattern. Facies II is also characterized by high peaks in Ti/K and Mn/Al ratios, associated with higher Q90/Q10 values. The transition between Facies II and III is gradual. Facies III is the coarsest interval of the T1-type beds. It consists of laminated and cross-laminated intervals (Fig. 4a). Sedimentary structures change upward from horizontal parallel laminations to oblique laminae then back to horizontal laminations. Cross-laminations are interpreted to have been formed during deposition of climbing ripples. Coarse fragments of organic-matter (100−300 µ) are abundant and organised following the sandy laminations (Fig. 4b). Similar distribution and orientation patterns are observed for primary minerals, particularly for micas recognised by their third-order birefringence, by typical phyllosilicate morphology and by EDX elemental analyses (Fig. 4c). Angular and sub-angular grains of quartz present common small to large conchoidal microfractures and V−shaped percussion cracks (Fig. 4d). The Ti/K ratio remains high and constant, and the Mn/Al ratio decreases in phase with the coarser material. The transition between Facies III and IV is marked by a sharp contact. Facies IV is a normally graded and laminated interval (Fig. 4a). Horizontal laminations thin and become fine upward. Additional features of Facies IV include an absence of clay and fine-silt material, high amounts of mica minerals and continental organic-matter fragments at the top. Both the Ti/K and Mn/Al ratios increase upward and suddenly decrease at the transition with the overlaying Facies V (Fig. 4a). The transition between Facies IV and V is sharp. Facies V is structureless or poorly-laminated (Fig. 4a). It consists of clay and fine-silt minerals mixed with coarse-grained particles, following a normal grading. Both the Ti/K and Mn/Al ratios decrease upward.

The identification of 83 T1 event-layers along the studied laminated interval is therefore based on a combination of Ti/K, Mn/Al and Q90/Q10 peaks. Thicker T1 events are bracketed by Mn/Al peaks (as shown in Fig. 4), while thin T1 events presented only punctual Mn/Al peaks, because of analysing resolution effect. The plot of Q90 versus Q50 (Fig. 6a) and grain-size distributions (Fig. 6c) shows two different groups of T1: the first one (T1α) with a Q90max of 100 µm and a Q50max of 12 µm and a bimodal distribution with a dominant mode at 20−30 µm; the second (T1β) with a Q90max of 50−250 µm and a Q50max of 12−100 µm and a bimodal distribution with the main well-sorted mode at 50−70 µm.

4.3.2. T2 event-layer description

The beds of type T2 (0.2−2 cm thick) are either massive or laminated silty to very-fine sand intervals (Fig. 5a, b, c), with a sharp basal contact, and are not composed of a superposition of subsequent facies. The clay fraction is abundant, while the coarse-grained fraction is well sorted. In contrast to T1 event-layers, the few organic-matter fragments follow random organisation and orientation patterns, while rare foraminifera and coccolithophore shells are fragmented (Fig. 5c). Within the whole sapropelic laminated interval (~7−10.5 ka BP), beds of type T2 are characterized by more or less pronounced Q90/Q10, Ti/K peaks and by the lack of or very low Mn/Al peaks (Figs. 3b and 6b). All these characteristics suggest a mixed material probably caused by reworked sediments. The plot of Q90 versus Q50 is mainly comprised between 60 µm (Q90max) and 40 µm (Q50; Fig. 6b and c) with a grain-size distribution similar to T1α beds (bimodal with a main mode around 20−30 µm).

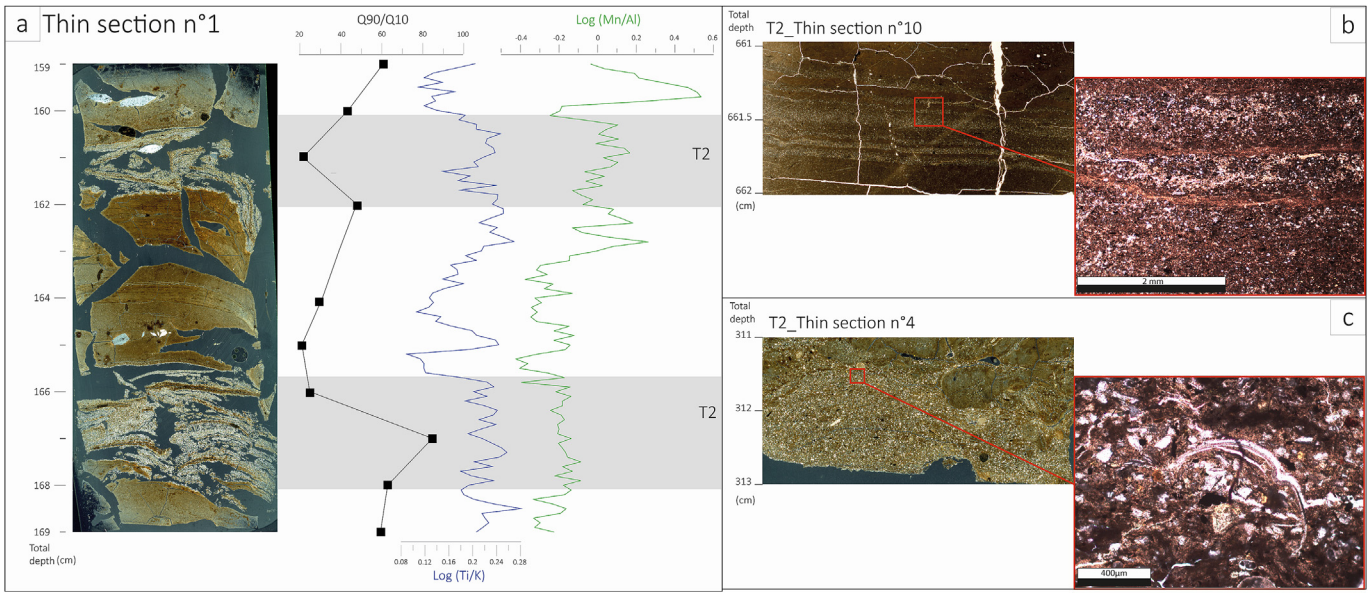

Fig. 5. a) Scan in crossed polarized light of thin section N°1 with T2 event-layer facies locations and Log (Ti/K) (blue line), Log (Mn/Al) (green line) and Q90/Q10 (black line). **b**) Light microscopy and scan images in plane polarized light of T2 facies and localisation of thin section N°10, showing a massive deposition of silty beds. **c**) Light microscopy and scan images in plane polarized light of T2 facies and location of thin section N°4, showing massive and reworked sediment and a fragmented foraminifer. (For interpretation of the references to colour in this figure legend, the reader is referred to the Web version of this article.)

5. Interpretations and discussion

Recurrent Nile exceptional floods trigger high detrital inputs in the Rosetta channel-levee system, resulting in the frequent occurrence of turbidites during the AHP (Fig. 3). Using a multi-proxy method, we are able to distinguish between deposits resulting from "classical" landslide-triggered turbidity currents and hyperpycnal flows (Sec 5.1). We present an estimation of the frequency of T1 hyperpycnal event-layers in core MD04-2726 which is compared with two well-dated sediment intervals already identified in cores from the Rosetta System (Sec. 5.2). Finally, from this comparison, we validate the reliability of the Nile flood frequency reconstruction at the scale of the Rosetta System and we propose a robust index of the exceptional flood frequency of the Nile River during the AHP (Sec. 5.3). We then discuss the timing and pattern of this flood frequency in comparison with hydro-climatic data from the Nile basin and East Africa.

5.1. T1 and T2 event-layers: interpretation and formation processes

The full T1 event-layers consist of the superposition of five intervals with different types of sedimentary structure and an inverse then normal grading (Fig. 4). In a turbidite system, superposition of an inverse then a normal grading reflects deposition by a waxing (accelerating) then waning (decelerating) flow. First, waxing flows can be generated both by an increasing slope angle and/or by an increasing entrainment of seafloor sediment. Because T1 event-layers were recovered from an almost-flat levee (Figs. 1a and 7b) on which overflow energy should be low, these two hypotheses of waxing flow formation processes are unlikely. Second, waxing flows can be generated at a river mouth during severe floods, such as hyperpycnal flows (Mulder et al., 2001). In this case, the mixed grading together with occurrence of sedimentary structures should record the rapid succession over time of a depletive waxing flow generated during river rise, and a depletive waning flow generated during river fall (Migeon et al., 2001; Mulder et al., 2001). T1 event-layers are similar in both grading and sedimentary structures to hyperpycnites first described in the Var Turbidite System (Migeon et al., 2001; Mulder et al., 2001).

Additional observations reinforce the flood-related hypothesis for T1 layers. The fluvial origin of T1 layers is supported by both sedimentological and geochemical tracers. First, quartz grains show small to large fresh conchoidal microfractures and V−shaped percussion cracks, typical of fluvial transfer processes (Fig. 5c; Vos et al., 2014). Furthermore, εNd values from T1 event-layers (−3 to −2) are systematically higher than corresponding hemipelagic sediments (Fig. 2b), indicating a large proportion of particles deriving from the Ethiopian Traps, which have εNd values of 0−7 (Fig. 8c, e; Ménot et al., 2020). Higher Ti/K ratios in T1 layers also support a higher contribution of basaltic rocks from the Ethiopian Traps, with primary minerals enriched in Ti, while secondary clay minerals are enriched in K (Croudace and Rothwell, 2015). The good correspondence between Ti/K and Q90/Q10 ratios suggests that the Ti/K ratio traces the silt versus clay fraction (Fig. 3b). In addition to coarser volcanic-derived particles, T1 event-layers contain large non-weathered mica minerals (>150 µm, Fig. 4b and c), which suggests a rapid terrigenous transfer from Blue Nile sources, potentially from the Dabus, Didesa (Blue Nile Basin) and Gash (Atbara basin) rivers (Fig. 1b; Garzanti et al., 2015).

Owing to this converging array of evidence, we propose that T1 event-layers represent the successive deposition of hyperpycnal flows overflowing on the right-hand levee of DSF6 (Fig. 7) during exceptional and near-instantaneous flooding events, which rapidly transferred sediments eroded in the Ethiopian Highlands to the western NDSF. This depositional model can even explain the difference observed between T1α and T1β layers (Figs. 6 and 7): during the low energy flood-induced phase, thin hyperpycnal flows are constrained at the channel floor, producing a graded-suspended sedimentation restricted to the levee crest (T1α). During the highest magnitude flood-induced flow phase, thick hyperpycnal flows expand within the whole channel conduit and overflow the levee crest, generating tractive processes that bring the coarsest grains over the levee area (T1β; Fig. 7).

In T1 event-layers, an increase of Mn/Al was systematically

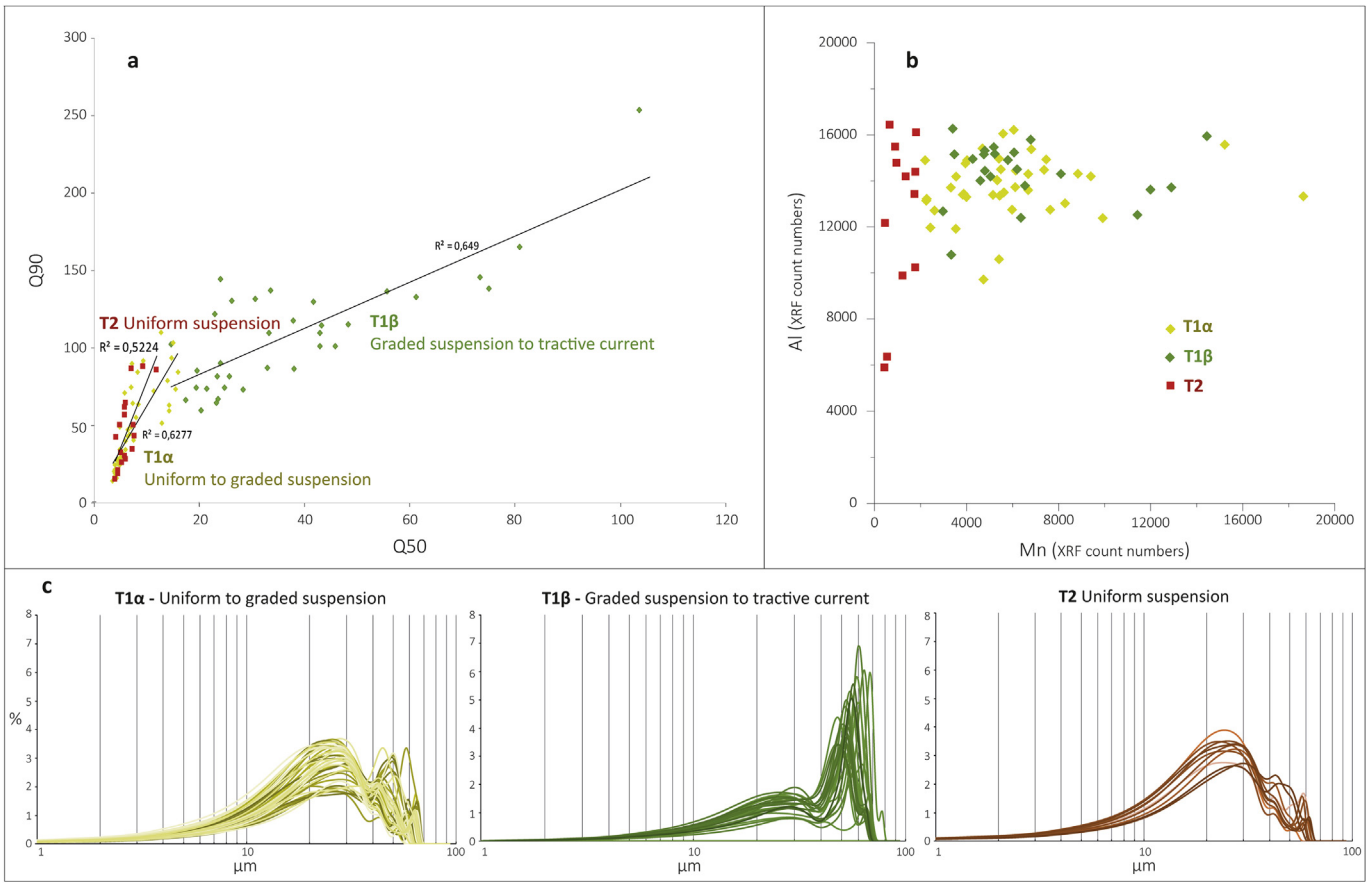

Fig. 6. a) Q90 versus Q50 plot of all the T1 and T2 event-layers from MD04-2726 core, showing the distinction between T1α types suggesting a uniform to graded suspension, and T1β types suggesting a graded suspension to tractive current sedimentation mode and T2 event-layers indicating a uniform to graded suspension sedimentation mode. **b**) Mn/Al plot (XRF count numbers) of T1α, T1β and T2 event-layers from III-IV-V sections of MD04-2726 core; **c**) Grain-size distribution of T1α, T1β and T2 event-layers (volume percentage vs. log of grain-size in µm) showing the grain-size sorting effect of the different sedimentation processes.

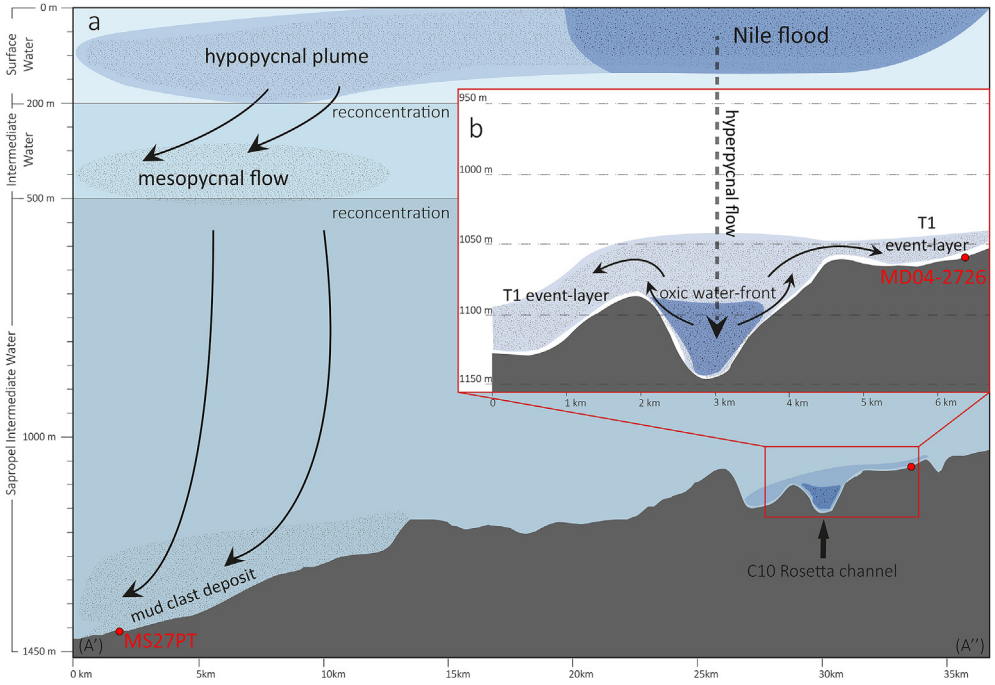

Fig. 7. a) Bathymetric profile of the proximal Rosetta upper slope (A′-A″, shown in Fig. 1a) with the positions of the MD04-2726 and MS27PT cores; the Sapropel Intermediate Water, Intermediate Water, Surface Water limits (after Zirks et al., 2019), and a schematic model of the formation process of the mud clast deposits (after Ducassou et al., 2009). **b**) Detail of the bathymetric profile of the C10 Rosetta channel (shown in Fig. 1a) with the position of the MD04-2726 core; and a schematic model of the formation process of the T1 event-layers (this study).

detected (Figs. 3, 4a and 6b). This enrichment in Mn might be related to the delivery of oxygen to the bottom waters by hyperpycnal flows (oxic freshwater front) that could be trapped in the porosity of the T1 beds. Mn would then be oxidized and precipitated in the form of Mn-oxyhydroxides (e.g. Deflandre et al., 2002; Torres et al., 2014; Wilhelm et al., 2016). Thus, we use here Mn/Al peaks as a marker of flood-induced deposit.

Regarding the T2 deposits, the presence of non-oriented organic matter, the more or less pronounced Ti/K ratios and the Q90/Q10 peaks suggest a continental origin, but the systematic absence of Mn/Al peaks (Figs. 3, 5a and 6b) also indicate a lack or lower amounts of fresh-water input. We propose that normally-graded T2 layers result from low-energy turbidity currents generated by landslides triggered at the Rosetta-Canyon head that reworked terrigenous and biogenic deposits from the outer continental shelf (Fig. 5c). This hypothesis seems to be confirmed by Q90/Q50 values in T2, which are consistent with uniform suspension processes resulting from a mixing of suspended material (Fig. 6b and c). T2 beds will thereafter be excluded from the climatic interpretations.

5.2. Coherence of Nile flood records over the upper slope of the Rosetta System

The frequency and the Nd isotopic signature of the hyperpycnal deposits (T1 event-layers recorded in MD04-2726 core) and clastic-mud beds (recorded in MS27PT core; Fig. 1a; Sup. Mat. Figs. S2 and S3 Fig. A2, A3) are compared, with the aim of testing the coherence of these different Nile flood records over the Rosetta upper slope. A similarity in elemental composition (increase of Ti/K and Mn/Al; Sup. Mat Fig. A3) a temporal coherence can be observed between the T1 event-layers and the clastic-mud deposits recorded in core MS27PT (Fig. 8d, f; Revel et al., 2015). During strong floods, two types of processes can be generated synchronously: a low-concentrated hypopycnal plume at the sea surface and a high-concentrated hyperpycnal flow plunging at the bottom (Mulder et al., 2003; Mulder and Alexander, 2001). During exceptional Nile floods, we therefore suggest that the resultant hyperpycnal flows are trapped within the Rosetta Canyon and channels and form T1 event-layers on levees (MD04-2726 core site). Low-density hypopycnal plumes spread at the sea surface while their fine-grained suspended particles are affected by decantation and convection processes along the water column, resulting in the deposition of clastic-mud beds over more than 30 km on the continental slope (MS27PT and PS3622-33core sites; Fig. 7; Ducassou et al., 2009). The exceptional nature of the T1α and T1β floods, occurring at an average of 1–7 events every 100 yr (Fig. 8b), suggests an intermittent high-energy hydrological activation. As described in detail in paragraph 5.1, T1β could indicate higher-energy floods than T1α event-layers.

5.3. Holocene hydro-climatic shifts over the Blue Nile basin

Our results document the frequency of exceptional (high-energy) Ethiopian Nile flood events during the Early and Middle Holocene (~10.1–~7.3 ka BP; Fig. 9e). This multi-centennial paleo-flood chronicle seems to be uniformly recorded in two piston-cores as hyperpycnal-flow deposits and clastic-mud beds over the proximal Rosetta System (western NDSF; Fig. 8). We compared this flood frequency record with the precipitation-induced runoff activity recorded at Lake Tana, as derived from the Ti concentration profile (Figs. 1b and 9g; Marshall et al., 2011), and with the K and Ti events recorded at Lake Dendi (Figs. 1b and 9f; Wagner et al., 2018) interpreted as an intense erosion and rainfall runoff at the head of the Blue Nile Basin. Precise correlation between single runoff and flood events would be hazardous because of the chronological uncertainty when comparing regional archives. However, general trends of the selected proxies seem to be coherent at centennial-scale.

Fluctuations of radiogenic εNd values in both T1 layers and hemipelagic sediments in all cores from the western NDSF (Fig. 9c and d, for MD04-2726 and MS27PT and Blanchet et al., 2014 for P362/2–33) reflect changes in the proportion of eroded material from Ethiopian Traps. Similar source-to-sink flood/runoff trends, combined with the high radiogenic εNd signature of T1 event-layers and clastic mud deposits (Fig. 9c and d) demonstrate the capacity of the Nile drainage system to rapidly connect the Ethiopian Traps source to its deep delta, and discredit the hypothesis of autogenic sediment transport anomalies (non-linear geomorphic system; Jerolmack and Paola, 2010). Decrease in εNd values could be explained by a higher contribution from the Equatorial-White Nile (African craton εNd = −30) or from the lower-course White/Blue Nile sources (Saharan Metacraton imprint; Abdelsalam et al., 2002; Grousset and Biscaye, 2005; Skonieczny et al., 2011). However, the Early to Mid-Holocene relative elevated εNd values of the silt fraction show that the proportion of Ethiopian Traps material remained high even during more arid periods (such as the 8.2 ka event; εNd = −4; Fig. 9c and d), hence clearly suggesting persistent inputs from the Ethiopian Traps and/or on-going sediment transport via the Blue Nile and the Sobat/Atbara rivers to the NDSF.

Based on correlation with other paleoclimatic and paleoenvironmental regional studies, the centennial time resolution of flood-induced event-layers reveals three trends in Early to Mid-Holocene hydro-climatic dynamics.

5.3.1. From 10 to 9 ka BP: a strong and stable hydro-climatic activity

From 10.1 to 9 ka BP, more radiogenic εNd values of hemipelagic sediment (around −4.5), T1 event-layers (−3 to −2; MD04-2726 core) and clastic mud beds from MS27PT core (−4 to −3, Fig. 9c and d) demonstrate the dominant contribution of Ethiopian Traps material to the sedimentation in the western NDSF. This is accompanied by high sedimentation rates in all three deltaic cores and therefore suggests major erosional activity in the Nile watershed (Figs. 1a, 8d and 8f). The paleo-flood frequency reconstruction shows a strong increase of the Nile River's hydrological activity from 10.1 ka BP onwards, which is in phase with maximal June insolation at 15°N (Fig. 9a). Exceptional Nile flood events culminate at 9.5–9 ka BP with seven high-energy floods every 100 yrs (Fig. 9e).

High precipitation-led runoff at Lake Dendi (Ti and K events, Fig. 9f, Wagner et al., 2018) and Lake Tana (Ti content, Fig. 9g, Marshall et al., 2011), both located at the source of the Blue Nile, seem to occur synchronously with intervals of the strongest Nile flood events (T1β layers; Fig. 9e). Additionally, continental geomorphological data from the Blue and White Nile lower courses (Khartoum region; Williams, 2009; Williams et al., 2015) seem coherent with our results: high energy exceptional T1β event-layers are in phase (within age uncertainty) with enhanced Nile flood periods recorded until 9 ka BP (Fig. 9h). This temporal coherency in runoff activity along the Nile River drainage basin suggests strong erosion dynamics from the source to the sink of the fluvial system.

This strong erosional activity during the Early Holocene occurs during an interval of intense monsoonal precipitations recorded from 10 ka BP onwards by low and constant δD_{wax} values at Lake Tana (Fig. 9b; Costa et al., 2014), Lake Victoria (Berke et al., 2012) and by stable high water-levels of East African lakes (Gasse, 2000; Junginger et al., 2014; Khalidi et al., 2020). We therefore propose the occurrence of enhanced erosional activity within the whole drainage basin of the Nile River during the Early Holocene, largely

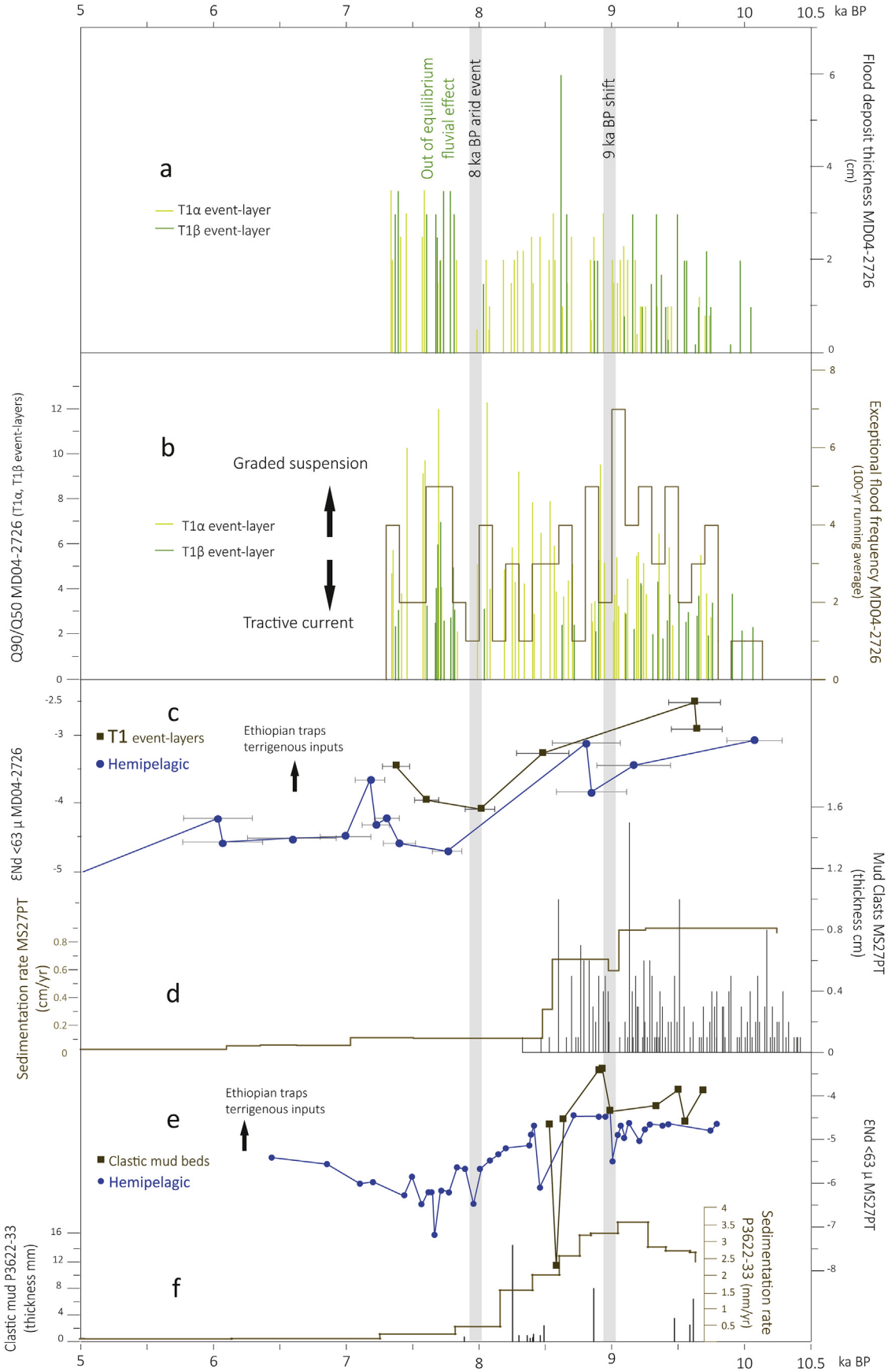

Fig. 8. a) Thickness of flood-induced deposits (cm; T1α in yellow and T1β in green) of the MD04-2726 core. **b)** Q90/Q50 ratio and frequency (100-yr running average, brown line) of flood deposits (T1α in yellow and T1β in green) of the MD04-2726 core. **c)** εNd of T1 event-layers (brown line and squares) and hemipelagic sediment (blue line and dots). **d)** Sedimentation rate (cm/yr, brown line) and thickness of mud clast deposits (T1α and T1β event-layers) of the MS27PT core. **e)** εNd of clastic mud deposits (brown line and squares) and of hemipelagic sediment (blue line and dots) from core MS27PT (fraction <63 μm; after Ménot et al., 2020; this study). **f)** Sedimentation rate (mm/yr, in brown) and thickness of mud clast deposits from the P3622-33 core. (For interpretation of the references to colour in this figure legend, the reader is referred to the Web version of this article.)

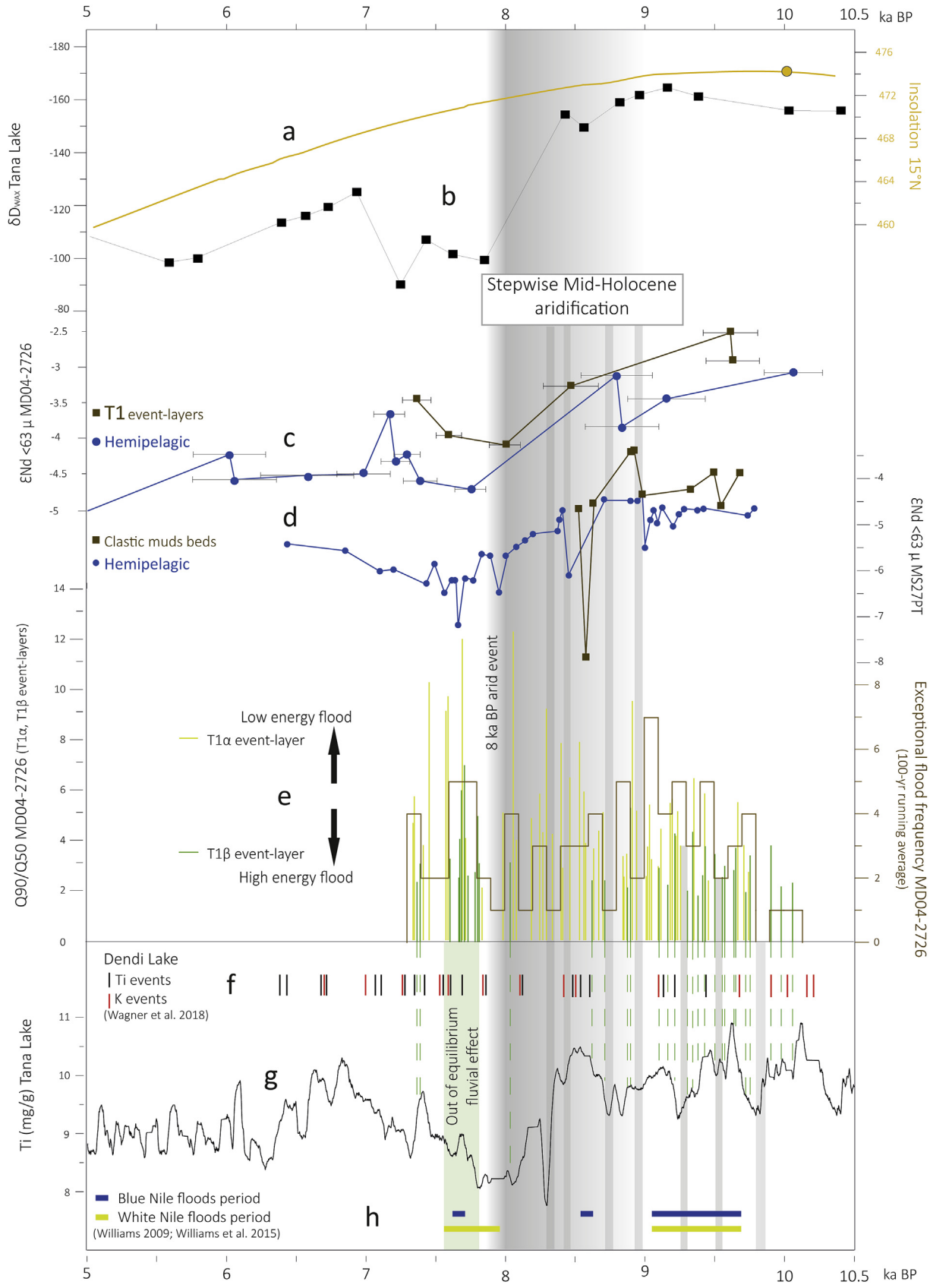

Fig. 9. Paleovariations from 10.5 to 5 ka BP of: **a**) July insolation at 15°N (Berger and Loutre, 1991); **b**) δD_{WAX} ( ) at Lake Tana (Costa et al., 2014); **c**) εNd of T1 event-layers (brown line and squares) and hemipelagic sediment (blue line and points) of the MD04-2726 core; **d**) εNd of clastic mud deposits (brown line and squares) and of hemipelagic sediment (blue line and dots) from core MS27PT (fraction <63 μm) (after Ménot et al., 2020; this study) **e)** Q90/Q50 and frequency (100-yr running average, brown line) of exceptional flood deposits (T1α in yellow and T1β in green) of the MD04-2726 core; **f**) erosion runoff-induced K and Ti event layers from Lake Dendi (Wagner et al., 2018); **g**) Ti (mg/g) at Lake Tana (Marshall et al., 2011); **h**) Blue (in blue) and White (in yellow) lower Nile course flood periods recorded over the Khartoum region (Williams, 2009; Williams et al., 2015). Light grey bands indicate the lower flood frequency recorded in MD04-2726 core. (For interpretation of the references to colour in this figure legend, the reader is referred to the Web version of this article.)

related to high and stable monsoonal rainfall on the Ethiopian Highlands.

5.3.2. Stepwise Early Holocene hydro-climatic degradation from 9 ka BP

From 9 ka BP onwards, εNd values of hemipelagic sediment and Ti layers from cores MD04-2726 and MS27PT start to decrease following the progressive decrease in frequency of T1 event-layers and of sedimentation rates in cores MS27PT and P362/2–33 (Fig. 8c–f). A lower frequency of T1α layers, rare T1β event-layers and less radiogenic εNd values indicate that Nile hydrologic activity had reduced very gradually from 9 until 7.8 ka BP, with an emphasis of reduction between 8.2 and 7.8 ka BP (Fig. 9c–e).

After a short-lived drop in flood frequency at 9 ka BP, the thickness of T1 event-layers and clastic-mud beds slightly decrease, indicating a reduction of flood particle discharge and/or shorter-lasting floods (Fig. 8a) while the higher Q90/Q50 ratio of T1 event-layers points to reduced flow energy (Fig. 8b). The combination of reduced flood particle discharge, weakened transport energy and decreasing flood frequency suggests a switch of the Nile River hydrological regime from episodic high-energy flood discharge dynamics (between 10 and 9 ka BP) to low-energy and shorter-lasting flood discharge dynamics (after 9 ka BP). This progressive shutdown of flood frequency and intensity, with more negative εNd, culminates between 8.2 and 7.8 ka BP, suggesting an ~800 year-long stepwise Early Holocene aridification interval (Fig. 9).

A distinct interruption of the Blue and White Nile flooding events was also recorded around 9 ka BP in the Khartoum region (Fig. 9h; Williams, 2009), in phase with an interruption of rainfall-induced runoff events at Lake Dendi (Fig. 9f; Wagner et al., 2018). Similarly, at Lake Tana a slight reduction in precipitations is evidenced by δD_{wax} values around 9 ka BP (Fig. 9b; Costa et al., 2014) interpreted as reflecting either a southward retreat of the monsoonal rain belt or an eastward shift of the Congo Air Boundary. Changes in erosion and monsoonal dynamics as early as ~8.7 ka BP have already been pointed out by previous studies (Blanchet et al., 2014; Ménot et al., 2020).

Subsequently, around 8.2 to 8 ka BP, a period of marked aridification was reported elsewhere in North East Africa as a single event (Costa et al., 2014; Garcin et al., 2012; Gasse, 2000; Marshall et al., 2011). A classical scenario suggests that high latitudes fully drove low-latitude hydrology at millennial timescales (Collins et al., 2017). The onset of aridification in the Nile catchment would then result from the release of freshwater in the North Atlantic during the 8.2 ka BP event, leading to a slowdown of the Atlantic Meridional Overturning Circulation (AMOC) and/or a decrease in arctic air temperatures which induces a decrease on the Tropical Easterly Jet (Collins et al., 2017). These processes, together with a reduction in summer insolation, might have led to drier conditions in tropical monsoonal areas.

However, this scenario does not account for a destabilization of the monsoonal system as early as 9 ka BP, as seen in our record. The observed time lag between the beginning of the hydrologic shift in East Africa at 9 ka BP and the North Atlantic 8.2 ka BP cooling event casts doubt on the mechanisms linking high- and low-latitude hydrological changes (Collins et al., 2017; Mohtadi et al., 2016). We propose here that an early shift of the main climatic boundaries above the Ethiopian Highlands (Costa et al., 2014) linked with the gradual decrease in summer insolation might have been sufficient to initiate a drier period in the tropics between 9 and 8 ka BP. Accordingly, recent modelling experiments suggest that an obliquity-driven change in insolation gradient at low latitudes might have directly enhanced monsoonal rainfall (Bosmans et al., 2015b; Mantsis et al., 2014). Consequently, the insolation on the tropics could have largely contributed in generating air moisture masses over the oceans without the influence of the indirect energy-balance inputs from high-latitude internal forcing and from North Atlantic ice-sea interactions (Bosmans et al., 2015b, 2015a; Clement et al., 2015). Finally, it has even been argued that the high-latitude cooling events would be further enhanced by the decrease in African precipitation and by Saharan aridification, which may have contributed to a tipping point behaviour between low and high latitudes (Clement et al., 2001; Davies et al., 2014).

5.3.3. Unstable and anomalous Nile hydrologic conditions from 7.8 ka BP

The low εNd values observed from 7.8 ka BP in both T1 layers and hemipelagic sediments in all cores from the western NDSF (Fig. 9c and d; for MD04-2726 and MS27PT and Blanchet et al., 2014 for P362/2–33) indicate a lower contribution of Ethiopian Trap detrital particles suggesting a White Nile or lower-course White and Blue Nile source contributions, characterized by a Saharan aeolian Metacraton imprint (εNd from −10 to −14; Abdelsalam et al., 2002; Grousset and Biscaye, 2005; Scheuvens et al., 2013).

After low flood activity around 8 ka BP, T1 event-layers resume from 7.8 ka BP onwards, with a frequency of five event-layers/100 yr, thereby characterizing higher particle discharge (increase in T1 thickness; Fig. 8a), reduced flow energy (increase of Q90/Q50 ratio produced by Q50 drop) and a reduction of Ethiopian Traps source inputs (lower εNd values; −4.5, Fig. 9c and d). Higher flood frequency is associated with a high amount of T1β layers until 7.6 ka BP, and a reduction of flood frequency to ca. 2.5 event-layers/100 yrs is associated with a dominance of T1α layers (Fig. 9e). Contemporarily, leaf wax deuterium isotopes at Lake Tana indicate lower precipitation over the Ethiopian Highlands, at the source of the Blue Nile (Fig. 9b; Costa et al., 2014).

The occurrence of higher flood frequency and higher particle discharge during a lower rainfall period shows a decoupling between erosive activity and climatic forcing, suggesting the development of an “out of equilibrium” geomorphic system (i.e., the sedimentary input into the system is not equal to the system output, Ahnert, 1994; Hoffmann, 2015). This anomaly could be explained by a process during the entire 8.2–7.8 ka BP arid period whereby low precipitation favoured fluvial riverbed aggradation (i.e., storage effect; Phillips, 2003). The subsequent slight resumption of precipitation post-7.8 ka BP (reduced δD_{WAX} at Lake Tana, Fig. 9b, f) led to a rapid erosion of the previously deposited sediment with low radiogenic εNd values along the Nile course, producing a dense plume at the river mouth and the large amount of T1 event-layers.

This is supported by other geomorphological data, which indicate the resumption of White Nile floods in the Khartoum region from 7.8 ka BP, in phase with the numerous low radiogenic T1 event-layers (Fig. 9h and e; Williams, 2009; Williams et al., 2015). Following this scenario, drastic reduction in vegetation cover over the Saharan Nile and the Sahelian belt (Hopcroft et al., 2017) during the 8.2 ka BP event could have accentuated this process with an enhanced soil erosion (Blanchet et al., 2014).

Our results therefore show how at the end of abrupt arid climatic events, such as those occurring around 8.2–7.8 ka BP, an “out of equilibrium” fluvial effect may occur, characterized by a disproportionate sediment delivery to the continental margins and resulting in an autogenic sedimentation process relatively decoupled from climatic forcing.

From 7 ka BP, re-oxygenation of bottom waters in the Levantine area mark the end of S1 (De Lange et al., 2008) and the end of the hyperpycnite-prone interval due to resumed bioturbation in MD04-2726 and MS27PT cores (Fig. 1d and e). The input of Blue Nile

suspended material, as well as the flood energy, decreased progressively until ~4 ka BP, thus preventing the formation of high dense plumes capable of inducing hyperpycnal flows. Accordingly, the lowest εNd and Ti/K values were measured from hemipelagic sediment (−6.5; Fig. 1b and c), corresponding to the ~4.2 ka BP drought event (Bini et al., 2019).

6. Conclusion

This study presents the first continuous reconstruction of exceptional Nile floods at centennial resolution from a well-preserved sedimentary interval from the Nile Deep-Sea Fan during the Early to the Middle Holocene. A multiproxy approach using sedimentological, geochemical (elemental contents and Nd isotopes) and microscopic methods have allowed us to identify instantaneous deposits (as hyperpycnites and clastic-mud beds) related to exceptional floods from the Blue Nile recorded in two cores from the upper slope of the Rosetta System. Similar trends between the occurrence of flood layers at centennial scale and changes in terrigenous input at Lake Tana (the source of the Blue Nile under direct influence of the African summer monsoon), as well their εNd signature, suggest their direct relationship to high-intensity and exceptional monsoon-related erosive and runoff events in the Ethiopian Highlands.

Our results enable us to draw some hydro-climatic inferences, in particular: **a**) the occurrence of recurrent (5–7/100 yr) high energy instantaneous floods between 10.1 and 9 ka BP during the height of the African Humid Period; **b**) a noticeable shift in the hydro-climatic regime around 9 ka BP characterized by a progressive reduction of Blue Nile input and by lower frequency and magnitude of floods until 8.2 ka BP; **c**) a low precipitation regime from 8.2 ka BP expressed in very low river runoff; **d**) the installation of an unstable and reduced Ethiopian-Nile hydrological regime from 7.8 ka BP where erosive activity and sediment transport is decoupled from climatic forcing, followed by a gradual reduction in precipitation intensity until ~4 ka BP.

In conclusion, we highlight the occurrence of a stepwise aridification process during the Early Holocene in the Blue Nile basin that questions the climatic linkages and feedbacks between low and high latitudes around the 8.2 ka BP North Atlantic cooling event. We also show how hyper-arid climatic episodes such as the 8.2 ka BP event might produce a destabilization of the fluvial geomorphic system, inducing an anomaly of sediment transfer and the consequent autogenic sediment recording over the continental margin basins.

Author statement

Carlo Mologni: Conceptualization, Investigation, Formal analysis, Data curation, Writing - original draft, Writing - review & editing, Resources. Marie Revel: Conceptualization, Investigation, Validation, Writing - review & editing, Supervision, Resources, Funding acquisition. Cécile Blanchet: Investigation, Writing - review & editing. Delphine Bosch: Investigation, Formal analysis, Writing - review & editing. Anne-Lise Develle: Formal analysis. François Orange: Investigation, Formal analysis, Writing - review & editing. Luc Bastian: Investigation. Lamya Khalidi: Writing - review & editing, Visualization, Supervision, Funding acquisition. Emmanuelle Ducassou: Writing - review & editing, Visualization. Sébastien Migeon: Investigation, Writing - original draft, Writing - review & editing, Validation, Resources, Supervision, Project administration, Funding acquisition. All these authors contributed to this work (see author statement) and approved the final version of the manuscript.

Declaration of competing interest

The authors declare that they have no known competing financial interests or personal relationships that could have appeared to influence the work reported in this paper.

Acknowledgments

Research at GEOAZUR laboratory (CNRS-UMR7329) was supported by a BQR-OCA, INSU-SYSTER (P.I. MR) and by the French government, through the UCAJEDI Investments in the Future project managed by the National Research Agency (ANR) with the reference number ANR-15-IDEX-01 (P.I. LK, co-P.I. MR). Nd measurement costs were partially covered by the program MADHO (INSU MISTRALS- P.I. MR) and by a BQR-0CA (Geoazur-P.I. MR). Radiocarbon dating of core MD04-2726 was performed by the national facility LMC14 in the framework of the INSU ARTEMIS grant scheme. We thank Jean-Pascal Dumoulin from LMC14 for discussions and Tomasz Goslar from the Poznan Radiocarbon Laboratory. We are grateful to Catherine Buchanan of the 'Office of International Scientific Visibility' of the UCA for the manuscript revision. We thank Aurélie Mothet and Sébastien Pivot for their Masters work on core MD04–2726 and M. Zanti for labwork support. Finally, the kind, thorough and constructive comments provided by Eduardo Garzanti, an anonymous reviewer and the editor Giovanni Zanchetta allowed to significantly improve the quality of this manuscript. We thank them for their time investment in these difficult circumstances (COVID-19 lockdown period).

Appendix A. Supplementary data

Supplementary data for this article can be found online at https://doi.org/10.1016/j.quascirev.2020.106543.

References

Abdelsalam, M.G., Liégeois, J.-P., Stern, R.J., 2002. The saharan Metacraton. J. Afr. Earth Sci. 34, 119–136. https://doi.org/10.1016/S0899-5362(02)00013-1.

Ahnert, F., 1994. Equilibrium, scale and inheritance in geomorphology. Geomorphology 11, 125–140. https://doi.org/10.1016/0169-555X(94)90077-9.

Bastian, L., Revel, M., Bayon, G., Dufour, A., Vigier, N., 2017. Abrupt response of chemical weathering to Late Quaternary hydroclimate changes in northeast Africa. Sci. Rep. 7, 44231. https://doi.org/10.1038/srep44231.

Bayon, G., German, C.R., Boella, R.M., Milton, J.A., Taylor, R.N., Nesbitt, R.W., 2002. An improved method for extracting marine sediment fractions and its application to Sr and Nd isotopic analysis. Chem. Geol. 187, 179–199. https://doi.org/10.1016/S0009-2541(01)00416-8.

Be'eri-Shlevin, Y., Avigad, D., Gerdes, A., 2018. The White Nile as a source for Nile sediments: assessment using U-Pb geochronology of detrital rutile and monazite. J. Afr. Earth Sci. 140, 1–8. https://doi.org/10.1016/j.jafrearsci.2017.12.032.

Berger, A., Loutre, M.F., 1991. Insolation values for the climate of the last 10 million years. Quat. Sci. Rev. 10, 297–317. https://doi.org/10.1016/0277-3791(91)90033-Q.

Berke, M.A., Johnson, T.C., Werne, J.P., Schouten, S., Sinninghe Damsté, J.S., 2012. A mid-Holocene thermal maximum at the end of the African Humid Period. Earth Planet Sci. Lett. 351–352, 95–104. https://doi.org/10.1016/j.epsl.2012.07.008.

Bini, M., Zanchetta, G., Perşoiu, A., Cartier, R., Català, A., Cacho, I., Dean, J.R., Di Rita, F., Drysdale, R.N., Finnè, M., Isola, I., Jalali, B., Lirer, F., Magri, D., Masi, A., Marks, L., Mercuri, A.M., Peyron, O., Sadori, L., Sicre, M.-A., Welc, F., Zielhofer, C., Brisset, E., 2019. The 4.2\,ka\,BP Event in the Mediterranean region: an overview. Clim. Past 15, 555–577. https://doi.org/10.5194/cp-15-555-2019.

Blaauw, M., Christen, J.A., 2011. Flexible paleoclimate age-depth models using an autoregressive gamma process. Bayesian Anal 6, 457–474. https://doi.org/10.1214/ba/1339616472.

Blanchet, C.L., 2019. A database of marine and terrestrial radiogenic Nd and Sr isotopes for tracing earth-surface processes. Earth Syst. Sci. Data 11, 741–759. https://doi.org/10.5194/essd-11-741-2019.

Blanchet, C.L., Frank, M., Schouten, S., 2014. Asynchronous changes in vegetation, runoff and erosion in the Nile river watershed during the Holocene. PloS One 9, 1–18. https://doi.org/10.1371/journal.pone.0115958.

Blanchet, C.L., Tjallingii, R., Frank, M., Lorenzen, J., Reitz, A., Brown, K., Feseker, T., Brückmann, W., 2013. High- and low-latitude forcing of the Nile River regime

during the Holocene inferred from laminated sediments of the Nile deep-sea fan. Earth Planet Sci. Lett. 364, 98–110. https://doi.org/10.1016/j.epsl.2013.01.009.
Bosmans, J.H.C., Drijfhout, S.S., Tuenter, E., Hilgen, F.J., Lourens, L.J., 2015a. Response of the North African summer monsoon to precession and obliquity forcings in the EC-Earth GCM. Clim. Dynam. 44, 279–297. https://doi.org/10.1007/s00382-014-2260-z.
Bosmans, J.H.C., Hilgen, F.J., Tuenter, E., Lourens, L.J., 2015b. Obliquity forcing of low-latitude climate. Clim. Past 11, 1335–1346. https://doi.org/10.5194/cp-11-1335-2015.
Bouvier, A., Vervoort, J.D., Patchett, P.J., 2008. The Lu–Hf and Sm–Nd isotopic composition of CHUR: constraints from unequilibrated chondrites and implications for the bulk composition of terrestrial planets. Earth Planet Sci. Lett. 273, 48–57. https://doi.org/10.1016/j.epsl.2008.06.010.
Bronk Ramsey, C.B., 2017. Methods for summarizing radiocarbon datasets. Radiocarbon 59, 1809–1833. https://doi.org/10.1017/RDC.2017.108.
Chalié, F., Gasse, F., 2000. Late Glacial Holocene diatom record of water chemistry and lake level change from the tropical East African Rift Lake Abiyata (Ethiopia). Palaeogeogr. Palaeoclimatol. Palaeoecol. 187, 259–283.
Chauvel, C., Blichert-Toft, J., 2001. A hafnium isotope and trace element perspective on melting of the depleted mantle. Earth Planet Sci. Lett. 190, 137–151. https://doi.org/10.1016/S0012-821X(01)00379-X.
Clement, A., Bellomo, K., Murphy, L.N., Cane, M.A., Mauritsen, T., Radel, G., Stevens, B., 2015. The Atlantic Multidecadal Oscillation without a role for ocean circulation. Science 350, 320–324. https://doi.org/10.1126/science.aab3980.
Clement, A.C., Cane, M.A., Seager, R., 2001. An orbitally driven tropical source for abrupt climate change. J. Clim. 14, 7.
Collins, J.A., Prange, M., Caley, T., Gimeno, L., Beckmann, B., Mulitza, S., Skonieczny, C., Roche, D., Schefuß, E., 2017. Rapid termination of the African Humid Period triggered by northern high-latitude cooling. Nat. Commun. 8, 1372. https://doi.org/10.1038/s41467-017-01454-y.
Collins, J.A., Schefuß, E., Heslop, D., Mulitza, S., Prange, M., Zabel, M., Tjallingii, R., Dokken, T.M., Huang, E., Mackensen, A., Schulz, M., Tian, J., Zarriess, M., Wefer, G., 2011. Interhemispheric symmetry of the tropical African rainbelt over the past 23,000 years. Nat. Geosci. 4, 42–45. https://doi.org/10.1038/ngeo1039.
Costa, K., Russell, J., Konecky, B., Lamb, H., 2014. Isotopic reconstruction of the african humid period and Congo air boundary migration at Lake Tana, Ethiopia. Quat. Sci. Rev. 83, 58–67. https://doi.org/10.1016/j.quascirev.2013.10.031.
Croudace, I.W., Rothwell, R.G. (Eds.), 2015. Micro-XRF Studies of Sediment Cores, Developments in Paleoenvironmental Research. Springer Netherlands, Dordrecht. https://doi.org/10.1007/978-94-017-9849-5.
Davies, F.J., Renssen, H., Blaschek, M., Muschitiello, F., 2014. The impact of Sahara desertification on Arctic cooling during the Holocene. Clim. Past Discuss 10, 1653–1673. https://doi.org/10.5194/cpd-10-1653-2014.
De Lange, G.J., Thomson, J., Reitz, A., Slomp, C.P., Speranza Principato, M., Erba, E., Corselli, C., 2008. Synchronous basin-wide formation and redox-controlled preservation of a Mediterranean sapropel. Nat. Geosci. 1, 606–610. https://doi.org/10.1038/ngeo283.
Deflandre, B., Mucci, A., Gagné, J.-P., Guignard, C., Sundby, B. jørn, 2002. Early diagenetic processes in coastal marine sediments disturbed by a catastrophic sedimentation event. Geochem. Cosmochim. Acta 66, 2547–2558. https://doi.org/10.1016/S0016-7037(02)00861-X.
deMenocal, P., Ortiz, J., Guilderson, T., Adkins, J., Sarnthein, M., Baker, L., Yarusinsky, M., 2000. Abrupt onset and termination of the African Humid Period: rapid climate responses to gradual insolation forcing. Quat. Sci. Rev. 19, 347–361.
Dewar, G., Reimer, P.J., Sealy, J., Woodborne, S., 2012. Late-Holocene marine radiocarbon reservoir correction (ΔR) for the west coast of South Africa. Holocene 22, 1481–1489. https://doi.org/10.1177/0959683612449755.
Ducassou, E., Capotondi, L., Murat, A., Bernasconi, S.M., Mulder, T., Gonthier, E., Migeon, S., Duprat, J., Giraudeau, J., Mascle, J., 2007. Multiproxy Late Quaternary stratigraphy of the Nile deep-sea turbidite system — towards a chronology of deep-sea terrigeneous systems. Sediment. Geol. 200, 1–13. https://doi.org/10.1016/j.sedgeo.2007.01.023.
Ducassou, E., Migeon, S., Mulder, T., Murat, A., Capotondi, L., Bernasconi, S.M., Mascle, J., 2009. Evolution of the Nile deep-sea turbidite system during the Late Quaternary: influence of climate change on fan sedimentation. Sedimentology 56, 2061–2090. https://doi.org/10.1111/j.1365-3091.2009.01070.x.
Ducassou, E., Mulder, T., Migeon, S., Gonthier, E., Murat, A., Revel, M., Capotondi, L., Bernasconi, S.M., Mascle, J., Zaragosi, S., 2008. Nile floods recorded in deep Mediterranean sediments. Quat. Res. 70, 382–391. https://doi.org/10.1016/j.yqres.2008.02.011.
Foerster, V., Junginger, A., Langkamp, O., Gebru, T., Asrat, A., Umer, M., Lamb, H.F., Wennrich, V., Rethemeyer, J., Nowaczyk, N., Trauth, M.H., Schaebitz, F., 2012. Climatic change recorded in the sediments of the Chew Bahir basin, southern Ethiopia, during the last 45,000 years. Quat. Int. 274, 25–37. https://doi.org/10.1016/j.quaint.2012.06.028.
Folk, R.L., Ward, W.C., 1957. Brazos river bar: a study in the significance of grain size parameters. J. Sediment. Petrol. 27, 3–26.
Garcin, Y., Melnick, D., Strecker, M.R., Olago, D., Tiercelin, J.-J., 2012. East African mid-Holocene wet–dry transition recorded in palaeo-shorelines of Lake Turkana, northern Kenya Rift. Earth Planet. Sci. Lett. 331– 332, 322–334. https://doi.org/10.1016/j.epsl.2012.03.016.
Garzanti, E., Andò, S., Padoan, M., Vezzoli, G., El Kammar, A., 2015. The modern Nile sediment system: processes and products. Quat. Sci. Rev. 130, 9–56. https://doi.org/10.1016/j.quascirev.2015.07.011.
Gasse, F., 2000. Hydrological changes in the african tropiccs since the last glacial maximum. Quat. Sci. Rev. 19, 189–211.
Grousset, F.E., Biscaye, P.E., 2005. Tracing dust sources and transport patterns using Sr, Nd and Pb isotopes. Chem. Geol. 222, 149–167. https://doi.org/10.1016/j.chemgeo.2005.05.006.
Hennekam, R., Donders, T.H., Zwiep, K., de Lange, G.J., 2015. Integral view of Holocene precipitation and vegetation changes in the Nile catchment area as inferred from its delta sediments. Quat. Sci. Rev. 130, 189–199.
Hoffmann, T., 2015. Sediment residence time and connectivity in non-equilibrium and transient geomorphic systems. Earth Sci. Rev. 150, 609–627. https://doi.org/10.1016/j.earscirev.2015.07.008.
Hopcroft, P.O., Valdes, P.J., Harper, A.B., Beerling, D.J., 2017. Multi vegetation model evaluation of the Green Sahara climate regime: rainfall supporting a green sahara. Geophys. Res. Lett. 44, 6804–6813. https://doi.org/10.1002/2017GL073740.
Jerolmack, D.J., Paola, C., 2010. Shredding of environmental signals by sediment transport: signal shredding. Geophys. Res. Lett. 37 https://doi.org/10.1029/2010GL044638 n/a-n/a.
Junginger, A., Roller, S., Olaka, L.A., Trauth, M.H., 2014. The effects of solar irradiation changes on the migration of the Congo Air Boundary and water levels of paleo-Lake Suguta, Northern Kenya Rift, during the African Humid Period (15–5ka BP). Palaeogeogr. Palaeoclimatol. Palaeoecol. 396, 1–16. https://doi.org/10.1016/j.palaeo.2013.12.007.
Khalidi, L., Mologni, C., Ménard, C., Coudert, L., Gabriele, M., Davtian, G., Cauliez, J., Lesur, J., Bruxelles, L., Chesnaux, L., Redae, B.E., Hainsworth, E., Doubre, C., Revel, M., Schuster, M., Zazzo, A., 2020. 9000 years of human lakeside adaptation in the Ethiopian Afar: Fisher-foragers and the first pastoralists in the Lake Abhe basin during the African Humid Period. Quat. Sci. Rev. 243, 1–24. https://doi.org/10.1016/j.quascirev.2020.106459.
Krom, M.D., Stanley, J.D., Cliff, R.A., Woodward, J.C., 2002. Nile River Sediment Fluctuations over the Past 7000 Yr and Their Key Role in Sapropel Development 5.
Mantsis, D.F., Lintner, B.R., Broccoli, A.J., Erb, M.P., Clement, A.C., Park, H.-S., 2014. The response of large-scale circulation to obliquity-induced changes in meridional heating gradients. J. Clim. 27, 5504–5516. https://doi.org/10.1175/JCLI-D-13-00526.1.
Marshall, M.H., Lamb, H.F., Huws, D., Davies, S.J., Bates, R., Bloemendal, J., Boyle, J., Leng, M.J., Umer, M., Bryant, C., 2011. Late pleistocene and Holocene drought events at Lake Tana, the source of the blue nile. Global Planet. Change 78, 147–161. https://doi.org/10.1016/j.gloplacha.2011.06.004.
Mascle, J., Sardou, O., Loncke, L., Migeon, S., Caméra, L., Gaullier, V., 2006. Morphostructure of the Egyptian continental margin: insights from swath bathymetry surveys. Mar. Geophys. Res. 27, 49–59. https://doi.org/10.1007/s11001-005-1559-x.
Ménot, G., Pivot, S., Bouloubassi, I., Davtian, N., Hennekam, R., Bosch, D., Ducassou, E., Bard, E., Migeon, S., Revel, M., 2020. Timing and stepwise transitions of the African Humid Period from geochemical proxies in the Nile deep-sea fan sediments. Quat. Sci. Rev. 228, 106071. https://doi.org/10.1016/j.quascirev.2019.106071.
Migeon, S., Ducassou, E., Le Gonidec, Y., Rouillard, P., Mascle, J., Revel-Rolland, M., 2010. Lobe construction and sand/mud segregation by turbidity currents and debris flows on the western Nile deep-sea fan (Eastern Mediterranean). Sediment. Geol. 229, 124–143. https://doi.org/10.1016/j.sedgeo.2010.02.011.
Migeon, S., Savoye, B., Zanella, E., Mulder, T., 2001. Detailed seismic-reection and sedimentary study of turbidite sediment waves on the Var Sedimentary Ridge (SE France): signi®cance for sediment transport and deposition and for the mechanisms of sediment-wave construction. Mar. Petrol. Geol. 30.
Mohtadi, M., Prange, M., Steinke, S., 2016. Palaeoclimatic insights into forcing and response of monsoon rainfall. Nature 533, 191–199. https://doi.org/10.1038/nature17450.
Mulder, T., Alexander, J., 2001. The Physical Character of Subaqueous Sedimentary Density ows and Their Deposits 31.
Mulder, T., Migeon, S., Savoye, B., Faugères, J.-C., 2001. Inversely graded turbidite sequences in the deep Mediterranean: a record of deposits from flood-generated turbidity currents? Geo Mar. Lett. 21, 86–93. https://doi.org/10.1007/s003670100071.
Mulder, T., Syvitski, J.P.M., Migeon, S., Faugères, J.-C., Savoye, B., 2003. Marine hyperpycnal flows: initiation, behavior and related deposits. A review. Mar. Petrol. Geol. 20, 861–882. https://doi.org/10.1016/j.marpetgeo.2003.01.003.
Mulitza, S., Prange, M., Stuut, J.-B., Zabel, M., von Dobeneck, T., Itambi, A.C., Nizou, J., Schulz, M., Wefer, G., 2008. Sahel megadroughts triggered by glacial slowdowns of Atlantic meridional overturning: sahel drought and atlantic overturning. Paleoceanography 23. https://doi.org/10.1029/2008PA001637 n/a-n/a.
Padoan, M., Garzanti, E., Harlavan, Y., Villa, I.M., 2011. Tracing Nile sediment sources by Sr and Nd isotope signatures (Uganda, Ethiopia, Sudan). Geochem. Cosmochim. Acta 75, 3627–3644. https://doi.org/10.1016/j.gca.2011.03.042.
Parsons, J.D., Bush, J.W.M., Syvitski, J.P.M., 2001. Hyperpycnal plume formation from riverine outflows with small sediment concentrations. Sedimentology 48, 465–478. https://doi.org/10.1046/j.1365-3091.2001.00384.x.
Phillips, J.D., 2003. Sources of nonlinearity and complexity in geomorphic systems. Prog. Phys. Geogr. Earth Environ. 27, 1–23. https://doi.org/10.1191/0309133303pp340ra.
Prospero, J.M., Ginoux, P., Torres, O., Nicholson, S.E., Gill, T.E., 2002. Environmental characterization of global sources of atmospheric soil dust identified with the

NIMBUS 7 Total Ozone Mapping Spectrometer (TOMS) absorbing aerosol product. Rev. Geophys. 40, 1–31. https://doi.org/10.1029/2000RG000095.
Reimer, P.J., Bard, E., Bayliss, A., Beck, J.W., Blackwell, P.G., Ramsey, C.B., Buck, C.E., Cheng, H., Edwards, R.L., Friedrich, M., Grootes, P.M., Guilderson, T.P., Haflidason, H., Hajdas, I., Hatté, C., Heaton, T.J., Hoffmann, D.L., Hogg, A.G., Hughen, K.A., Kaiser, K.F., Kromer, B., Manning, S.W., Niu, M., Reimer, R.W., Richards, D.A., Scott, E.M., Southon, J.R., Staff, R.A., Turney, C.S.M., van der Plicht, J., 2013. IntCal13 and Marine13 radiocarbon age calibration curves 0–50,000 Years cal BP. Radiocarbon 55, 1869–1887. https://doi.org/10.2458/azu_js_rc.55.16947.
Reimer, P.J., McCormac, F.G., Moore, J., McCormick, F., Murray, E.V., 2002. Marine radiocarbon reservoir corrections for the midto late Holocene in the eastern subpolar North Atlantic. Holocene 12, 129–135. https://doi.org/10.1191/0959683602hl528rp.
Reimer, R.W., Reimer, P.J., 2017. An online application for dr calculation. Radiocarbon 59, 1623–1627. https://doi.org/10.1017/RDC.2016.117.
Revel, M., Colin, C., Bernasconi, S., Combourieu-Nebout, N., Ducassou, E., Grousset, F.E., Rolland, Y., Migeon, S., Bosch, D., Brunet, P., Zhao, J., Mascle, J., 2014. 21,000 Years of Ethiopian African monsoon variability recorded in sediments of the western Nile deep-sea fan. Reg. Environ. Change 14 (5), 1685–1696. https://doi.org/10.1007/s10113-014-0588-x.
Revel, M., Ducassou, E., Grousset, F.E., Bernasconi, S.M., Migeon, S., Revillon, S., Mascle, J., Murat, A., Zaragosi, S., Bosch, D., 2010. 100,000 Years of African monsoon variability recorded in sediments of the Nile margin. Quat. Sci. Rev. 29, 1342–1362. https://doi.org/10.1016/j.quascirev.2010.02.006.
Revel, M., Ducassou, E., Skonieczny, C., Colin, C., Bastian, L., Bosch, D., Migeon, S., Mascle, J., 2015. 20,000 years of Nile River dynamics and environmental changes in the Nile catchment area as inferred from Nile upper continental slope sediments. Quat. Hist. River Nile 130, 200–221. https://doi.org/10.1016/j.quascirev.2015.10.030.
Rohling, E.J., Pälike, H., 2005. Centennial-scale climate cooling with a sudden cold event around 8,200 years ago. Nature 434, 975–979. https://doi.org/10.1038/nature03421.
Rossignol-Strick, M., Nesteroff, W., Olive, P., Vergnaud-Grazzini, C., 1982. After the deluge: Mediterranean stagnation and sapropel formation. Nature 295, 105–110. https://doi.org/10.1038/295105a0.
Santisteban, J.I., Mediavilla, R., López-Pamo, E., Dabrio, C.J., Blanca Ruiz Zapata, M., José Gil García, M., Castaño, S., Martínez-Alfaro, P.E., 2004. Loss on ignition: a qualitative or quantitative method for organic matter and carbonate mineral content in sediments? J. Paleolimnol. 32, 287–299. https://doi.org/10.1023/B:JOPL.0000042999.30131.5b.
Schefuß, E., Eglinton, T.I., Spencer-Jones, C.L., Rullkötter, J., De Pol-Holz, R., Talbot, H.M., Grootes, P.M., Schneider, R.R., 2016. Hydrologic control of carbon cycling and aged carbon discharge in the Congo River basin. Nat. Geosci. 9, 687–690. https://doi.org/10.1038/ngeo2778.
Scheuvens, D., Schütz, L., Kandler, K., Ebert, M., Weinbruch, S., 2013. Bulk composition of northern African dust and its source sediments — a compilation. Earth Sci. Rev. 116, 170–194. https://doi.org/10.1016/j.earscirev.2012.08.005.
Shanahan, T.M., McKay, N.P., Hughen, K.A., Overpeck, J.T., Otto-Bliesner, B., Heil, C.W., King, J., Scholz, C.A., Peck, J., 2015. The time-transgressive termination of the african humid period. Nat. Geosci. 8, 140–144. https://doi.org/10.1038/ngeo2329.
Siani, G., 2001. Mediterranean sea surface radiocarbon reservoir age changes since the last glacial maximum. Science 294, 1917–1920. https://doi.org/10.1126/science.1063649.
Skonieczny, C., Bory, A., Bout-Roumazeilles, V., Abouchami, W., Galer, S.J.G., Crosta, X., Stuut, J.-B., Meyer, I., Chiapello, I., Podvin, T., Chatenet, B., Diallo, A., Ndiaye, T., 2011. The 7–13 March 2006 major Saharan outbreak: multiproxy characterization of mineral dust deposited on the West African margin. J. Geophys. Res. 116, D18210. https://doi.org/10.1029/2011JD016173.
Skonieczny, C., McGee, D., Winckler, G., Bory, A., Bradtmiller, L.I., Kinsley, C.W., Polissar, P.J., De Pol-Holz, R., Rossignol, L., Malaizé, B., 2019. Monsoon-driven Saharan dust variability over the past 240,000 years. Sci. Adv. 5, eaav1887 https://doi.org/10.1126/sciadv.aav1887.
Skonieczny, C., Paillou, P., Bory, A., Bayon, G., Biscara, L., Crosta, X., Eynaud, F., Malaizé, B., Revel, M., Aleman, N., Barusseau, J.-P., Vernet, R., Lopez, S., Grousset, F., 2015. African humid periods triggered the reactivation of a large river system in Western Sahara. Nat. Commun. 6, 8751. https://doi.org/10.1038/ncomms9751.
Thomson, J., Mercone, D., De Lange, G.J., Van Santvoort, P.J.M., 1999. Review of recent advances in the interpretation of eastern Mediterranean sapropel S1 from geochemical evidence. Mar. Geol. 153, 77–89. https://doi.org/10.1016/S0025-3227(98)00089-9.
Tierney, J.E., deMenocal, P., 2013. Abrupt shifts in horn of Africa hydroclimate since the last glacial maximum. Science 342, 843–846. https://doi.org/10.1126/science.1244809.
Torres, N.T., Och, L.M., Hauser, P.C., Furrer, G., Brandl, H., Vologina, E., Sturm, M., Bürgmann, H., Müller, B., 2014. Early diagenetic processes generate iron and manganese oxide layers in the sediments of Lake Baikal, Siberia. Env. Sci Process. Impacts 16, 879–889. https://doi.org/10.1039/C3EM00676J.
Verschuren, D., Sinninghe Damsté, J.S., Moernaut, J., Kristen, I., Blaauw, M., Fagot, M., Haug, G.H., van Geel, B., De Batist, M., Barker, P., Vuille, M., Conley, D.J., Olago, D.O., Milne, I., Plessen, B., Eggermont, H., Wolff, C., Hurrell, E., Ossebaar, J., Lyaruu, A., van der Plicht, J., Cumming, B.F., Brauer, A., Rucina, S.M., Russell, J.M., Keppens, E., Hus, J., Bradley, R.S., Leng, M., Mingram, J., Nowaczyk, N.R., 2009. Half-precessional dynamics of monsoon rainfall near the East African Equator. Nature 462, 637–641. https://doi.org/10.1038/nature08520.
Viste, E., Sorteberg, A., 2013. Moisture transport into the Ethiopian highlands. Int. J. Climatol. 33, 249–263. https://doi.org/10.1002/joc.3409.
Vos, K., Vandenberghe, N., Elsen, J., 2014. Surface textural analysis of quartz grains by scanning electron microscopy (SEM): from sample preparation to environmental interpretation. Earth Sci. Rev. 128, 93–104. https://doi.org/10.1016/j.earscirev.2013.10.013.
Wagner, B., Wennrich, V., Viehberg, F., Junginger, A., Kolvenbach, A., Rethemeyer, J., Schaebitz, F., Schmiedl, G., 2018. Holocene rainfall runoff in the central Ethiopian highlands and evolution of the River Nile drainage system as revealed from a sediment record from Lake Dendi. Global Planet. Change 163, 29–43. https://doi.org/10.1016/j.gloplacha.2018.02.003.
Weldeab, S., Emeis, K.-C., Hemleben, C., Vennemann, T.W., Schulz, H., 2002. Sr and Nd isotope composition of Late Pleistocene sapropels and nonsapropelic sediments from the Eastern Mediterranean Sea: implications for detrital influx and climatic conditions in the source areas. Geochem. Cosmochim. Acta 66, 3585–3598. https://doi.org/10.1016/S0016-7037(02)00954-7.
Weltje, G.J., Tjallingii, R., 2008. Calibration of XRF core scanners for quantitative geochemical logging of sediment cores: theory and application. Earth Planet Sci. Lett. 274, 423–438. https://doi.org/10.1016/j.epsl.2008.07.054.
Wilhelm, B., Vogel, H., Crouzet, C., Etienne, D., Anselmetti, F.S., 2016. Frequency and intensity of palaeofloods at the interface of Atlantic and Mediterranean climate domains. Clim. Past 12, 299–316. https://doi.org/10.5194/cp-12-299-2016.
Williams, M.A.J., 2009. Late pleistocene and Holocene environments in the Nile Basin. Global Planet. Change 69, 1–15. https://doi.org/10.1016/j.gloplacha.2009.07.005.
Williams, M.A.J., Usai, D., Salvatori, S., Williams, F.M., Zerboni, A., Maritan, L., Linseele, V., 2015. Late Quaternary environments and prehistoric occupation in the lower White Nile valley, central Sudan. Quat. Sci. Rev. 130, 72–88. https://doi.org/10.1016/j.quascirev.2015.03.007.
Zirks, E., Krom, M.D., Zhu, D., Schmiedl, G., Goodman-Tchernov, B.N., 2019. Evidence for the presence of oxygen-depleted sapropel intermediate water across the eastern mediterranean during sapropel S1. ACS Earth Space Chem 3, 2287–2297. https://doi.org/10.1021/acsearthspacechem.9b00128.